Title

A Broadband Laboratory Study of the Seismic Properties of Cracked and Fluid-Saturated Synthetic Glass Media

Journal

Journal of Geophysical Research: Solid Earth, 123(5)

ISSN

2169-9313

Authors

Li, Yang

David, Emmanuel C

Nakagawa, Seiji

et al.

Publication Date

2018-05-01

DOI

10.1029/2017jb014671

Peer reviewed

A Broadband Laboratory Study of the Seismic Properties of Cracked and Fluid-Saturated Synthetic Glass Media

Yang Li[1] , Emmanuel C. David[1,2], Seiji Nakagawa[3] , Timothy J. Kneafsey[3] , Douglas R. Schmitt[4,5] , and Ian Jackson[1]

[1] Research School of Earth Sciences, Australian National University, Canberra, ACT, Australia, [2] Now at Department of Earth Sciences, University College London, London, UK, [3] Energy Geosciences Division, EESA, Lawrence Berkeley National Laboratory, Berkeley, CA, USA, [4] Department of Physics, University of Alberta, Edmonton, Alberta, Canada, [5] Now at Earth, Atmospheric, and Planetary Sciences Department, Purdue University, West Lafayette, IN, USA

Correspondence to: I. Jackson, ian.jackson@anu.edu.au

Abstract

For better understanding of frequency dependence (dispersion) of seismic wave velocities caused by stress-induced fluid flow, broadband laboratory measurements were performed on a suite of synthetic glass media containing both equant pores and thermal cracks. Complementary forced oscillation, resonant bar, and ultrasonic techniques provided access to millihertz-hertz frequencies, ~1 kHz frequency, and ~1 MHz frequency, respectively. The wave speeds or effective elastic moduli and associated dissipation were measured on samples under dry, argon- or nitrogen-saturated, and water-saturated conditions in sequence. The elastic moduli, in situ permeability, and crack porosity inferred from in situ X-ray computed tomography all attest to strong pressure-induced crack closure for differential (confining-minus-pore) pressures <30 MPa, consistent with zero-pressure crack aspect ratios $<4 \times 10^{-4}$. The low permeabilities of these materials allow access to undrained conditions, even at subhertz frequencies. The ultrasonically measured elastic moduli reveal consistently higher shear and bulk moduli upon fluid saturation—diagnostic of the saturated-isolated regime. For a glass rod specimen, containing cracks but no pores, saturated-isolated conditions apparently persist to subhertz frequencies—requiring in situ aspect ratios (minimum/maximum dimension) $<10^{-5}$. In marked contrast, the shear modulus measured at subhertz frequencies on a cracked glass bead specimen of 5% porosity, is insensitive to fluid saturation, consistent with the Biot-Gassmann model for the saturated-isobaric regime. The measured dispersion of the shear modulus approaches 10% over the millihertz-megahertz frequency range for the cracked and fluid-saturated media—implying that laboratory ultrasonic data should be used with care in the interpretation of field data.

1 Introduction

Seismic exploration of the Earth's crust and sonic logging are typically performed at frequencies of tens of hertz to a few kilohertz in the field,

whereas laboratory measurements of seismic properties are performed mainly at megahertz frequency with the well-established methods of ultrasonic wave propagation. The direct application of such ultrasonic measurements to field data acquired at much lower frequencies requires that seismic properties are nondispersive. However, stress-induced fluid flow induced by seismic waves in a cracked medium is expected to result in frequency dependence of seismic properties. A better understanding of stress-induced fluid flow during the propagation of seismic waves in the cracked and fluid-saturated upper crust therefore offers the prospect of more robust seismological interpretations.

The influence of fluid saturation on the seismic properties of cracked and/or porous media has been the subject of wide-ranging theoretical study. The family of “macroscopic” models based on poroelastic theory was initially developed by Gassmann (1951) at zero frequency and extended by Biot (1956a, 1956b) to higher frequencies. Subsequently, Mavko and Jizba (1991), Dvorkin and Nur (1993), Dvorkin et al. (1994, 1995), and Gurevich et al. (2010) incorporated the influence of “squirt” flow, as originally proposed by Mavko and Nur (1975), for a unified model of Biot and squirt-flow dispersion. In contrast, in effective medium theory, individual inclusions with assigned geometries are embedded within a solid to estimate the overall elastic properties of the composite from the elastic properties of individual constituents (Eshelby, 1957; Kachanov, 1993; Kuster & Toksöz, 1974; Wu, 1966; Zimmerman, 1991). Consideration of frequency-dependent fluid communication between the isolated fluid phases of conventional effective medium models provides insight into the dispersion of fluid-saturated medium and the influence of microstructure on dispersion (Adelinet et al., 2011; Chapman et al., 2002; Endres & Knight, 1997; Guéguen & Sarout, 2011; O'Connell & Budiansky, 1977).

Such theories (e.g., O'Connell & Budiansky, 1977; Sarout, 2012) provide an experimentally testable framework comprising conceptually distinct regimes of stress-induced fluid flow (Figure 1). A series of fluid flow regimes from *drained*, through *saturated isobaric*, to *saturated isolated* is expected with increasing frequency, separated by characteristic draining frequency f_{dr} and squirt flow frequency f_{sq}.

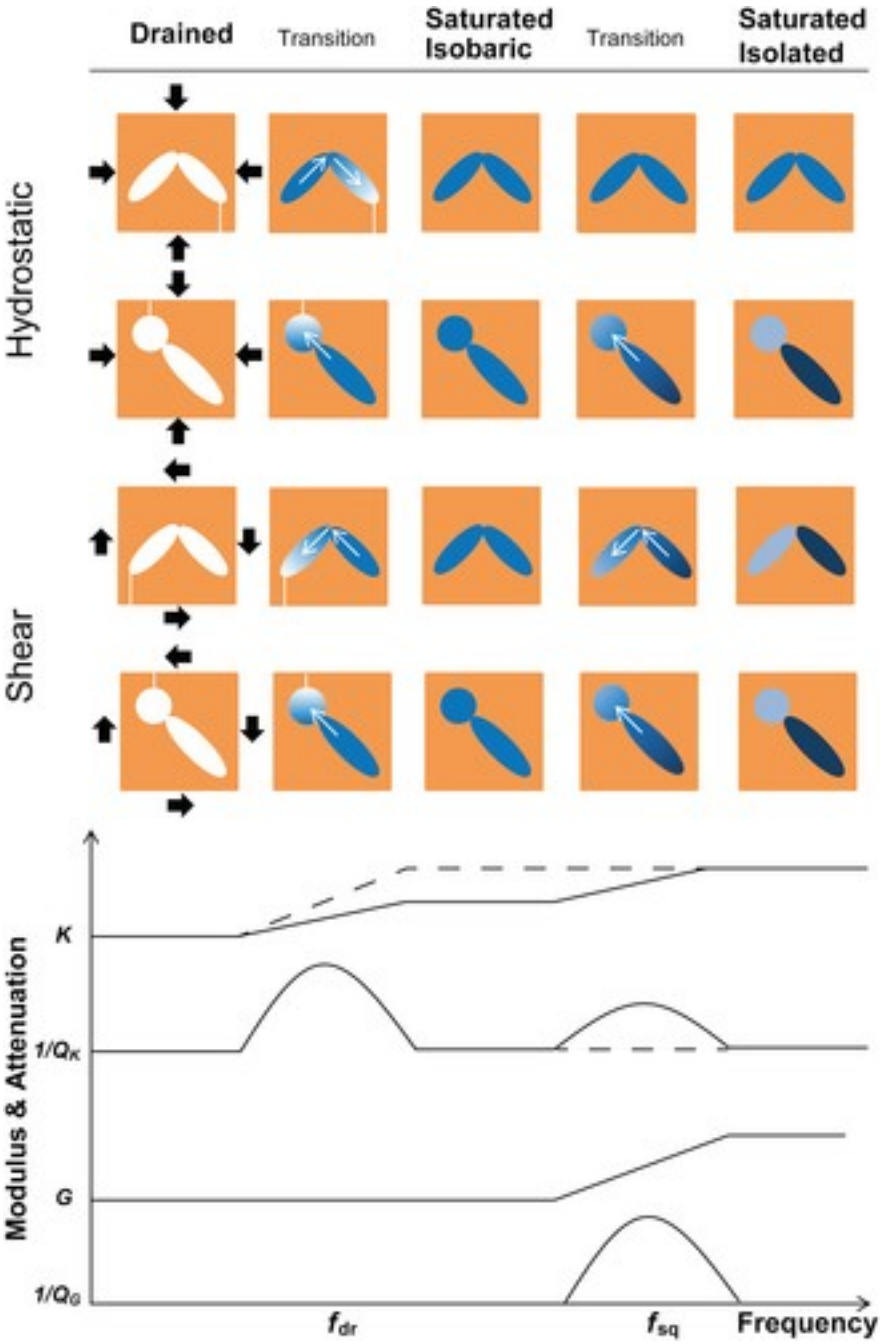

Figure 1

Stress-induced fluid flow regimes under externally imposed hydrostatic or shear stress: with increasing frequency, the drained, saturated isobaric, and saturated isolated regimes. Two types of inclusion are considered: cracks only and a combination of cracks and more nearly equant and therefore less compressible pores. The intensity of the color in each inclusion indicates the magnitude of the pressure, with a darker color corresponding to a higher pressure. Fluid flow and its direction during transition are indicated by arrows in the connected inclusions. The change in effective modulus and attenuation reflecting the transitions between fluid flow regimes are also indicated (after Jackson's, 1991, visualization of the model of O'Connell & Budiansky, 1977). The dashed trends for K and $1/Q_K$ versus frequency relate to material containing inclusions only of a single aspect ratio for which there are no stress-induced gradients in pore pressure within the specimen, and therefore no squirt flow.

In the drained regime, encountered at frequencies below f_{dr}, the pore pressure within the sample is uniform but (global) flow can occur between the rock's network of cracks and pores and an external reservoir. As a result, the fluid-saturated medium responds to an applied stress as if it were completely dry (assuming chemical interactions between rock and fluid are negligible). The bulk and shear moduli in this regime are the “drained” or “frame” moduli $K_d$and G_d, respectively, which are sometimes assumed equivalent to the “dry” moduli. At f_{dr}, the global fluid flow responsible for “drainage” of the rock subjected to an oscillating compressive stress component results in an attenuation peak associated with the bulk modulus.

If the excitation frequency is higher than f_{dr} but lower than f_{sq}, the fluid-saturated rock is in the saturated isobaric regime within which the pore pressure is uniform within an elementary volume that is representative of the crack-pore microstructure. The elastic moduli for this regime are given by the Biot-Gassmann low-frequency theory, where the incompressibility of the saturant must now be included—predicting an “undrained” bulk modulus K_u that is greater than the drained bulk modulus, but a shear modulus that is unchanged upon fluid saturation. A third behavioral transition from the saturated isobaric regime to the saturated isolated regime involves squirt flow between adjacent inclusions, indicated by a shear attenuation peak and an attenuation peak associated with hydrostatic compression reflecting any flow between differentially pressurized fluid inclusions of different aspect ratio. At frequencies greater than $f_{sq,}$ even local squirt flow is inhibited with no fluid transfer allowed between neighboring inclusions. The transition from saturated isobaric to saturated isolated regime gives an increase in shear modulus and a possible increase in bulk modulus.

The experimental study of dispersion of seismic properties of fluid saturated rocks involves the use of various dynamic methods for determination of the elastic moduli or wave velocities at relevant frequencies. The conventional ultrasonic wave propagation method has been widely applied on fluid saturated rocks. Comparison of ultrasonic results with the Biot-Gassmann zero-frequency prediction has revealed dispersion of seismic properties between zero and megahertz frequencies (King & Marsden, 2002; King et al., 2000; Winkler, 1985, 1986). Resonant bar methods provide access to the kilohertz frequencies employed by crosshole and borehole vertical seismic profiling in the field and have been well developed and applied to study the fluid flow related dispersion (Cadoret et al., 1995; Jones & Nur, 1983; Murphy, 1982, 1984; O'Hara, 1985, 1989; Winkler & Nur, 1982; Yin et al., 1992). Frequencies between 1 kHz and 100 kHz are also accessible, at least at ambient conditions, through differential acoustic resonance spectroscopy (Wang et al., 2011; Zhao et al., 2013, 2015) and resonant ultrasound spectroscopy (Ulrich et al., 2002; Zadler et al., 2004). An acoustic pulse tube method has been demonstrated for measurements on

unconsolidated marine sediments at elevated pressures to ~25 MPa and frequencies in the range 1–10 kHz (McCann et al., 2014).

Forced oscillation techniques provide access to even lower seismic frequencies (millihertz-hertz), relevant to the transition between saturated isobaric and drained conditions. Such techniques may involve uniaxial extensional/compressional mode oscillation (Adam & Batzle, 2008; Adam et al., 2006, 2009; Adelinet et al., 2010; Batzle et al., 2006; David et al., 2013; Delle Piane et al., 2014; Dunn, 1986, 1987; Fortin et al., 2014; Mikhaltsevitch et al., 2014; Spencer, 1981; White, 1986) or torsional oscillation (e.g., Lu & Jackson, 2006). A recently developed technique involving seismic frequency (0.004–0.4 Hz) oscillation of confining pressure (Adelinet et al., 2010; David et al., 2013; Pimienta et al., 2015a) has allowed unambiguous demonstration of the draining transition in glycerine-saturated Fontainebleau sandstones by relating dispersion of moduli and associated attenuation peaks with fluid pressure oscillations in an external reservoir connected to the sample pore space (Pimienta et al., 2015a).

Most past studies have focused on natural geological materials, especially sandstones for their economic importance as hydrocarbon reservoirs. However, the microstructural complexity of natural rocks makes it difficult to isolate and identify the physical mechanism of interest. Accordingly, synthetic samples with controlled microstructure have also been prepared and tested (Amalokwu et al., 2014; Ding et al., 2014; Rathore et al., 1994; Tillotson et al., 2012; Wang et al., 2015). Soda-lime-silica glass beads have been used either loose (Domenico, 1977; Wyllie et al., 1956) or after sintering (Bouzidi & Schmitt, 2009; Johnson & Plona, 1982; Palciauskas, 1992; Plona, 1980) to simulate porous reservoir rocks.

In the following, we will present a series of modulus measurements conducted over a broad frequency band, by the collaborating research institutions (see also Schijns et al., 2018). For the first time, forced oscillation, resonant bar, and ultrasonic wave propagation methods are combined in a broadband study of synthetic soda-lime-silica glass samples of controlled microstructure. We will first describe the methodology employed in fabrication and characterization of the glass media, the experimental procedures for the measurement of permeability, strain, and elastic moduli and strain energy dissipation within the different frequency bands, and the theoretical basis for the interpretation of the experimental observations. Subsequently, the results of all measurements are presented in graphical format. The full set of tabulated data is accessible in Li (2016), and a preliminary account of part of this work was presented by Li et al. (2014). Finally, the results obtained in this paper, along with related observations, are used to test the theoretical predictions of Figure 1concerning fluid flow regimes and related dispersion and attenuation in fractured media.

2 Specimen Preparation and Characterization

2.1 Sample Fabrication Procedure

Soda-lime-silica glass with its high silica content (~70–80 wt%) serves as a useful synthetic analog for sandstone. Moreover, its high thermal expansivity relative to fused silica (quartz glass), for example, is conducive to thermal cracking. Synthetic samples, with three types of microstructure, were fabricated in this study. The first type of sample termed “glass rod” was made from fully dense soda-lime-silica glass supplied by Nadège Desgenétez of the Glass Workshop, School of Art, Australian National University. In order to introduce equant pores, another type of synthetic sample was fabricated by sintering loose soda-lime-silica glass beads of similar chemical composition. Glass beads normally used for sand blasting were supplied by the Engineering Workshop, Research School of Earth Sciences, Australian National University. Chemical compositions of the glass rod and glass bead materials were determined by electron microprobe and scanning electron microscope (SEM) energy dispersive X-ray analysis.

Glass beads were sieved to diameters between 300 and 350 μm and loaded into a cylindrical mould of 100 mm height and 22 mm internal diameter, fitted with a thin aluminum liner. Vibration of the sintering jig results in compaction of the glass beads thereby minimizing potential spatial variability of porosity. Sintering, driven by reduction of surface energy through coalescence of adjacent beads, was achieved during a dwell at 700 °C for 18 hr, above the glass transition temperature of 500–600 °C. The sintered glass bead specimens were slowly cooled from 700 °C to room temperature by following a protocol (Li, 2016) designed to avoid thermal cracking. The result was a residual porosity of ~2% equant pores. Specimens of ~5% residual porosity were similarly prepared from glass beads sieved to 180–211 μm diameter.

Both glass rod and glass bead specimens were precision ground into cylinders of length and diameter suited to the various mechanical testing techniques described below. Selected precision-ground specimens were gradually heated to 500 °C for 2 hr and then quenched horizontally into liquid water at room temperature to introduce thermal cracks while maintaining overall mechanical integrity. Following such thermal treatment, each of the glass specimens contains a population of thin cracks, expected to be highly compliant under imposed pressure. Precise mensuration prior to and following thermal cracking provided robust estimates of the resulting crack porosity.

2.2 Sample Characterization: The Measurement of Porosity

2.2.1 Light Microscopy, Mensuration, and He Pycnometry

Optical microscopy is commonly used to determine the porosity of a cylindrical specimen from a transverse section (Dullien, 1992; Guéguen & Palciauskas, 1994). Sections were prepared from each end of each glass bead specimen and examined under a light microscope with the area of interest imaged and recorded by a digital camera for further image processing and analysis. To achieve statistical significance, multiple

microscopic images were taken from each section. The porosity, that is, the volume fraction of pores, can be approximated by the fraction ϕ_{op} of section area occupied by pores, provided that the distribution of pores is random.

Whereas the optical method thus allows estimation of the equant porosity, the crack porosity ϕ_{cr}, thermally induced in the glass specimens, is determined through precise mensuration of a precision-ground cylinder before and after thermal cracking. Average crack apertures and lengths, determined from light micrographs, are used to estimate average crack aspect ratios. It is noted that the surface of the sample cross section has been well polished before being examined by optical microscopy. The rounding of crack edges during polishing may result in systematic overestimation of crack apertures and hence crack aspect ratios.

The total porosity of a sample consists of both equant porosity and crack porosity, however, not all the equant pores are connected by cracks. The connected porosity ϕ_{He} can be determined by helium pycnometry. The total porosity ϕ_{total} is related to the connected porosity as

$$\phi_{He} < \phi_{total} = \phi_{op} + \phi_{cr}. \quad (1)$$

2.2.2 X-ray Computed Tomography

Information concerning the pressure-induced variation of porosity was obtained by X-ray computed tomography (CT) conducted in parallel with the resonant bar measurements at the Lawrence Berkeley National Laboratory. CT scanning was performed using a modified GE Lightspeed 16-slice medical CT scanner at an energy of 120 kV and 160 mA current. The scanner provides data in Hounsfield units which can be converted to density, and hence porosity, by also scanning a number of known density objects. The contrast in X-ray absorption between CT measurements on a dry cracked glass rod specimen at atmospheric pressure and at the maximum experimental pressure (25 MPa) provides an estimate of the amount of closable porosity. Voxel size for the CT scanning was 193 × 193 × 625 microns with the 625 micron dimension in the axial direction. The sample was contained within a thin poly-vinyl chloride (PVC) sleeve between resonance bar endpieces suspended from a cage and contained in a carbon fiber wound aluminum pressure vessel. The pressure vessel was mounted to the CT scanner table to reduce the need for image registration. In spite of that, some sample translation occurs due to table movement on successive scans and to the addition of effective stress; thus, registration is required to align the data stacks to allow computation of porosity. No registration was performed in the axial direction, and registration in the axis perpendicular direction was performed by inserting a “registration standard slice” into the same location in each stack. *Stackreg* (Thévenaz et al., 1998) was used to register the data stacks implemented in *ImageJ* (Schneider et al., 2012).

2.3 Characterization of Thermal Crack Networks

Besides the residual porosity of the sintered glass bead specimens, thermally introduced cracks and their geometric arrangements are also important in interpreting the observed dispersion and dissipation. Finite element modeling of the cylindrically symmetric thermal stress field during quenching glass cylinders from high temperature suggests that high tensile stresses are encountered near the surfaces of the cooling specimen in the circumferential, axial, and radial directions (Ougier-Simonin et al., 2011)—potentially causing preferred orientation of the resulting thermal cracks. Axial tensile stress should tend to produce cracks contained in planes transverse to the axis of the cylinder (type A), which would be most clearly visible in longitudinal cross section. The circumferential tensile stress during quenching should tend to produce cracks within planes containing both the longitudinal and radial axes of the sample (type B), visible in transverse cross section. Radial tensile stresses acting on the ends of the specimen during quenching should tend to create ring or “onion skin” cracks (type C), propagating longitudinally inward from the ends of the specimen, visible near the ends of the specimen in both longitudinal and transverse sections.

The lengths and apertures of cracks can be estimated from the images taken by light microscopy. A conventional petrographic microscope provides a good resolution and estimation of the crack aperture. However, the field of view of a conventional optical microscope is limited, and the image at the edge of the field of view is typically distorted. For this reason, a mosaic optical microscope was used to image entire transverse and longitudinal cross sections with even illumination and without distortion. A faint grid typically superimposed on such images is the legacy of assembling the individual images into the mosaic. Finally, the ratio between the mean aperture and the mean length of cracks on a cross section provides an estimate of the average crack aspect ratio α, and hence the crack density parameter Γ, defined more formally in equation A2 as $\Gamma = 3\phi_c/4\pi\alpha$.

3 Experimental Methodology

3.1 The Measurement of Permeability

3.1.1 The Steady State Flow Method

The steady state flow method, based on Darcy's law, was used in conjunction with the resonant bar method (described below) of the Lawrence Berkeley National Laboratory, on the cracked glass rod specimen. After the specimen was installed in the experimental apparatus, the fractures in the specimen were first saturated with water. This was done by cyclically applying vacuum to the pore space and flushing it with CO_2 gas (at ~0.4 MPa) for a few times under ~0.9 MPa of confining pressure. Because of the high solubility of CO_2 in water, this procedure minimizes the trapped residual gas in the fractures. After the final vacuuming step, a constant pressure gradient of pore water was applied and maintained across the sample at several confining stresses, with the water pressure on one end of the sample maintained at 3.45 MPa by a servo-controlled water pump, whereas the

other end was open to the atmosphere (0.1 MPa) through a piece of rubber tubing. The advance of the water front within the transparent tubing is monitored to provide a measure of the flux. The permeability of the sample is calculated from the known pore pressure gradient and fluid viscosity.

3.1.2 The Transient Flow Method

The transient flow method of Brace et al. (1968), well suited to less permeable rocks, was used on the “attenuation apparatus” (at the Australian National University) with argon as pore fluid (Lu & Jackson, 2006). A sample is sandwiched between upper and lower pore fluid reservoirs. In such a pore pressure equilibration experiment, an initial equilibrium between the two pore fluid reservoirs (in both pore pressure and temperature) was perturbed by introducing a small pressure increment/decrement (normally less than 5 MPa) to either the upper or lower reservoir. The return of the pore pressure to equilibrium is monitored until a common pore pressure is re-established between two reservoirs. The permeability k is calculated from the rate constant A for exponential decay of the imposed pore pressure differential as

$$k = A\eta L_s / \left[K_f A_s \left(V_u^{-1} - V_d^{-1}\right)\right] \quad (2)$$

where L_s and A_s are the length and cross-sectional area of the specimen, K_f and η are the bulk modulus and viscosity of the pore fluid, and $V_d \sim 40$ cm^3 and $V_u \cong 1.55(10)$ cm^3 are the volumes of the lower and upper reservoirs, respectively (Li, 2016; Lu & Jackson, 2006). As a routine prelude to forced oscillation testing, this process of pore pressure re-equilibration ensures uniform pore fluid pressure through the specimen.

3.2 Mechanical Testing

In order to provide a broadband assessment of the mechanical properties, the same or comparable samples were measured with each of the following techniques.

3.2.1 Forced Oscillation Technique

Access to millihertz-hertz frequencies, logarithmically equispaced between 0.01 and 0.26 Hz, was provided in forced oscillation tests performed on the “attenuation apparatus” (Jackson et al., 2011; Jackson & Paterson, 1993) at the Australian National University (Figure 2). The specimen, with unknown elastic moduli and of 150 mm length and 15 mm diameter, is composed of either a single cylinder (of glass rod material) or a stack of three similarly prepared glass bead cylinders each of 50 mm length. The specimen assembly, inclusive of glass cylinder(s) and hollow connecting rods of alumina or steel, is jacketed and sealed within a thin-walled (0.27 mm) sleeve of annealed copper. The pressure differential between the argon confining medium (to 150 MPa in this study) and the pore fluid, acting across each interface, ensures frictional coupling both within the specimen assembly and with an elastic element of known elastic moduli. The compound experimental assembly is subject to periodically varying torque or

bending force applied by a pair of electromagnetic drivers mounted near its lower end. Displacements associated with the torsional or flexural distortion of the specimen assembly and of the elastic element are measured by pairs of three-plate capacitance transducers located above and below the elastic element (Figure 2). The ratio of the complex torsional distortions of the specimen assembly and elastic element, extracted from the raw displacement time series by Fourier analysis, provides an estimate of the torsional compliance of the specimen assembly. Subtraction of the torsional compliance of a reference assembly, involving identical connecting rods and a control specimen of known modulus, from that of the specimen assembly, eliminates the contributions of the common series components including any interfacial compliance associated with the frictional coupling. For the low-porosity glass bead specimen, the reference assembly included alumina connecting rods and a two-piece fused silica control specimen, whereas in the later tests on the other specimens, the reference assembly involved steel connecting rods and the corresponding intact glass material as control specimen. Established procedures, including modeling of the compliance of the enclosing copper jacket, were used to extract from the comparative complex torsional compliances of the specimen assembly and reference assembly, the shear modulus, and associated strain energy dissipation of the specimen itself (Jackson & Paterson, 1993).

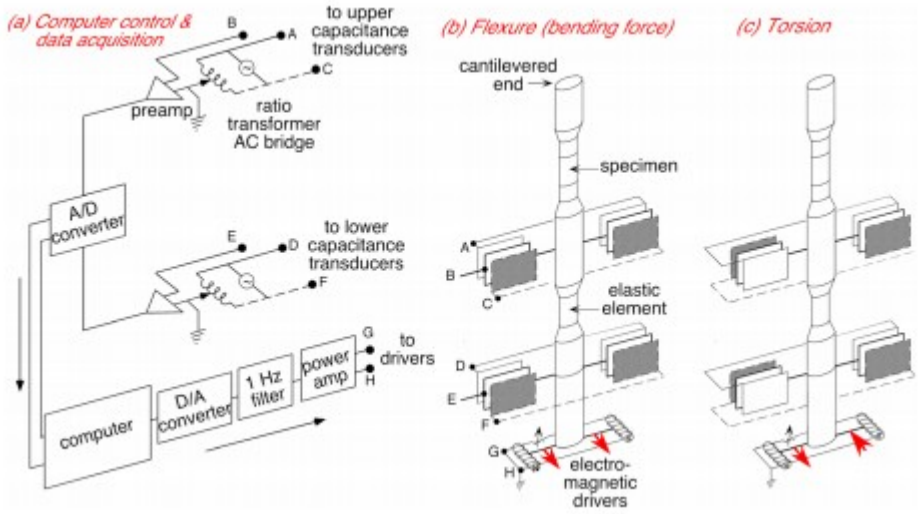

Figure 2

Experimental arrangements for forced oscillation tests at millihertz-hertz frequencies. (a) Computer control and data acquisition, (b) flexural (bending force), and (c) torsional modes with alternative configurations of electromagnetic drivers and displacement transducers. The experimental assembly illustrated in panels (b) and (c) is accommodated within a purpose-designed close-fitting argon-charged pressure vessel with independent control of confining and pore pressures (after Jackson et al., 2011).

Increased clearance between the lower end of the experimental assembly and the enclosing pressure vessel now allows flexural oscillation driven by a bending force (Figure 2b) rather than the previously used bending moment

(Jackson et al., 2011). The lower end of the long, thin, compound cylindrical beam (Figure 2) is accordingly now anchored to the enclosing pressure vessel by a compliant spiral vent tube whose flexural rigidity is established through prior calibration. The differential equation, governing the flexure of the beam in the filament elongation approximation, is solved with a finite difference approach (Jackson et al., 2011). Recent refinements include application of appropriate cantilevered boundary conditions at each end of the beam and its division into a larger number $N \sim 4{,}000–5{,}000$ of equal submillimeter intervals, with N chosen so that the length of the model vent tube is closely matched to an integral number of intervals (Cline II & Jackson, 2016). In this way, changes in Young's modulus associated with fluid saturation of the glass specimens are well resolved, although there remains substantial uncertainty in their absolute values, pending further improvement of the modeling procedures. The capacity to conduct such flexural oscillation measurements with an oscillating bending force is dependent upon closely coaxial alignment of the experimental assembly and the pressure vessel—a condition not always realized in practice. Accordingly, flexural measurements on the glass rod specimen were precluded although torsional tests were unaffected by the poor alignment. The independently controlled confining and pore fluid pressure systems allow in situ measurements of both mechanical and hydraulic properties of a specimen. The highest pore fluid pressure employed in this study was ~90 MPa.

The data acquisition system on the attenuation apparatus has been upgraded during this study. An 18-bit DAQ card (High-accuracy M series Multifunction NI PCI-6281 National Instruments®) has been installed with a new *LabVIEW* system to replace the previous 12-bit analog-to-digital converter, in order to minimize the quantization error and hence improve the signal-to-noise ratio. A new strategy of digital low-pass filtering has also been implemented for the data acquisition system, with a cutoff frequency that varies with imposed oscillation frequency. In the upgraded system, remote switching between the different electrical connections of transducer elements and driver units required for torsional and flexural oscillation modes is achieved by computer keyboard activation of relays within a *LabVIEW*operating environment.

3.2.2 Resonant Bar Method

The Split Hopkinson resonant bar method (Nakagawa, 2011; Nakagawa et al., 2013), implemented at the Lawrence Berkeley National Laboratory, United States, provides access to kilohertz frequencies. Measurements of the extensional and torsional resonance frequencies of a cylindrical specimen coupled with a pair of stainless steel extension bars yield the Young's and shear moduli and associated strain energy dissipations. A specimen of 38.1 mm in diameter and 76.2 mm in length was jacketed with a PVC heat shrink tubing and sandwiched between the pair of extension bars to form an integral bar under confining pressure (<30 MPa) provided by compressed nitrogen (Figure 3). Thin lead foils (~25 μm in thickness) were placed at the

interfaces between the specimen and extension bars in order to achieve improved mechanical coupling between the specimen and extension bars. Extension/compression- and torsion-mode sources and receivers, consisting of mode-specific piezoelectric ceramics, are mounted on the outer ends of the extension bars.

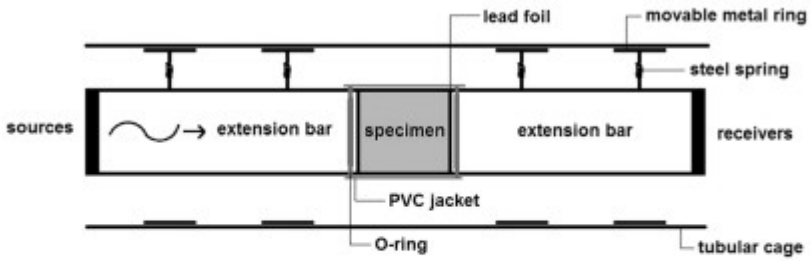

Figure 3. The specimen-bar assembly for the Split Hopkinson Resonant Bar tests at frequencies in the range 1–3 kHz. The assembly is suspended within a pressure vessel to provide independently controlled confining and pore fluid pressures.

Input signals (either chirp or random signals with desired range of frequencies) were generated by a fast Fourier transform (FFT) analyzer to excite the piezoelectric ceramics, thereby driving forced vibration of the specimen bar assembly. The signals detected by the accelerometers mounted on the other end of the specimen bar assembly, after proper conditioning and amplification, were received by the same FFT analyzer. The central frequency and width of the resonance peak provide the resonance frequency and attenuation, respectively. The use of extension bars allows the use of relatively short core samples for conducting the kilohertz range seismic measurements, at the cost of requiring a one-dimensional wave propagation model to determine the *P* and *S* wave velocities from the measured resonance frequencies (Nakagawa, 2011; Nakagawa et al., 2013). Minor distortion of resonance peak shapes resulting from interference between the extensional, flexural, and torsional modes results in estimated uncertainties of 1% in the resulting elastic moduli.

The apparatus has an independently controlled pore fluid pressure system, allowing use of either nitrogen or tap water as pore fluid. Nitrogen pore fluid was introduced from the gas reservoir directly until the target pore fluid pressure was reached. A servo-controlled fluid pump with adjustable injection rate was used with water pore fluid. Pore-fluid inlet and outlet lines were fed through the upper closure of the pressure vessel and through the extension bars to either end of the specimen, allowing circulation of pore fluid through the specimen.

3.2.3 Ultrasonic Wave Speed Measurements

Ultrasonic wave speed measurements, performed at the University of Alberta, provide access to elastic properties at frequencies near 1 MHz. The

ultrasonic wave propagation method is the most mature and widely used laboratory technique for studies of rock elasticity. In this method, a cylindrical specimen with a length of 50 mm and a diameter of 15 mm (identical with, or similarly prepared to, those tested in forced oscillation) was sandwiched between a pair of aluminum buffer caps with an attached stack of *P* and *S* wave ceramics to serve as source or receiver. The specimen was jacketed with PVC tubing to isolate the specimen from hydraulic oil as confining-pressure medium (to 100 MPa). The pore pressure system was independently controlled with either argon or water as pore fluid with the maximum pore fluid pressure of 40 MPa. The travel time of either *P* or *S* wave was compared with a calibration measurement determining the corresponding travel time in the pair of end caps only under the same pressure conditions, to provide the travel time of the wave through the sample alone. For calculation of wave speeds from measured travel times, pressure-induced changes in path length are ignored, so that the *P* and *S* wave speeds are systematically overestimated—but by no more than a negligible amount reaching 0.1% at 100 MPa. Shear and Young's moduli with uncertainties ~1% are calculated from the inferred wave speeds and the zero-pressure matrix density, adjusted as required for the pressure dependent density of the fluid saturant.

Strain gauge measurements on the samples were undertaken within the same apparatus used for ultrasonic wave speed measurement. A pair of perpendicularly oriented Omega® SGD-10/350-LY41 linear strain gauges, glued directly to the outer surface of the specimen inside the PVC jacket, provided the axial and circumferential strains for selected combinations of confining and pore pressures simultaneously with the ultrasonic wave speed determinations using procedures described in Melendez-Martinez and Schmitt (2016).

4 Theoretical Background

4.1 Inversion of Pressure-Dependent Elastic Properties of a Dry Cracked Medium for Crack Density and Crack/Pore Aspect Ratio Distribution

The strong pressure sensitivity of elastic moduli or wave speeds measured on cracked media is commonly attributed to the presence at low pressure of open compliant cracks and their progressive closure with increasing pressure. For such pressure-induced closure of a thin spheroidal crack of aspect ratio α (minor/major axis), the required pressure P_c is (Walsh, 1965)

$$P_c \approx E\alpha, \qquad (3)$$

where *E* is the Young's modulus of the “matrix” (formed by the minerals and any nonclosable, “equant” pores). Hence, quantitative modeling of the pressure-dependent elastic moduli of a cracked sample relative to its intact counterpart can provide insight into the distribution of aspect ratios for cracks and pores. The elastic moduli of a cracked medium, containing cracks of only relatively low aspect ratio, increase with increasing pressure before

reaching a plateau indicative of essentially complete crack closure. However, more nearly equant pores, with aspect ratios approaching unity, are hardly affected by pressure. The presence of such residual (“nonclosable”) porosity accounts for the modulus deficit relative to the mineral modulus, measured at the highest pressure P_{max} reached in an experiment. The geometry, that is, effective aspect ratio, of the nonclosable porosity at P_{max} can be inferred from the magnitudes of the high-pressure deficits in elastic moduli.

We employ a differential effective medium model (David, 2012; David & Zimmerman, 2011, 2012) in which both cracks with a distribution of aspect ratios and more nearly equant pores are modeled as spheroidal inclusions. Specifically, cracks of relatively low aspect ratio are embedded within a background medium that includes the nonclosable pores. The modeling strategy for obtaining the distribution of crack aspect ratios involves two main steps, details of which are given in Appendix Appendix A:

1. Crack density is independently inferred at each pressure from elastic moduli deficits relative to the high-pressure, “background medium”;
2. The pressure-dependent crack density thus obtained is then used to calculate the crack aspect ratio distribution (at zero pressure).

4.2 Modeling the Effect of Fluid Saturation on Elastic Moduli

4.2.1 Stress-Induced Fluid Flow Regimes

The bulk modulus is expected to increase on fluid saturation of an undrained medium because the incompressibility of the fluid tends to resist a net reduction in volume of the rock matrix, thereby increasing the overall bulk modulus of the medium (Biot, 1956a, 1956b; Gassmann, 1951). In contrast, whether or not the shear modulus is increased by fluid saturation depends on the maintenance or otherwise of stress-induced gradients in pore pressure within the fluid-saturated crack network and may thus be time or frequency dependent (Figure 1). The Biot-Gassmann theory (for the “saturated isobaric” regime of O'Connell & Budiansky, 1977) predicts a shear modulus unaffected by fluid saturation for low-frequency undrained conditions, based on zero net volume change for the connected inclusions under an externally imposed shear stress. However, at sufficiently short timescales (high frequencies) there will be insufficient time for relaxation by local squirt flow (Mavko & Nur, 1975) of stress-induced gradients in pore pressure between parts of the crack-pore network of different orientation and/or aspect ratio—conditions diagnostic of the “saturated isolated” regime (O'Connell & Budiansky, 1977). The existence of unrelaxed pore pressure gradients will result in higher shear moduli than for the saturated isobaric regime, and for a distribution of aspect ratios higher bulk moduli as well.

4.2.2 Characteristic Frequencies for Draining and Squirt Flow

It has long been predicted that mechanical testing at progressively increasing frequency will probe a succession of fluid flow regimes, separated

by characteristic frequencies (Figure 1). Based on the work of Cleary (1978) and Zimmerman (1991), the analysis given in Appendix Appendix B leads to the following limiting forms for the draining frequency f_{dr}, in constrasting situations in which the total pore compressibility $C_t = C_f + C_{pp}$ is dominated by either the pore fluid compressibility C_f or the pore compressibility C_{pp}, respectively:

$$f_{dr} \cong kK_f/\phi\eta l^2 \text{ for } C_f \gg C_{pp} \quad (4a)$$

$$f_{dr} \cong [3/8(1-\nu)]kG/\eta\Gamma l^2 \text{ for } C_{pp} \gg C_f. \quad (4b)$$

where k is rock permeability, $K_f = C_f^{-1}$, ϕ is porosity, η is the shear viscosity of the pore fluid, (ν, G) are respectively rock Poisson's ratio and shear modulus, Γ is crack density, and l is the length scale over which pore fluid diffusion occurs. The former situation (equation 4a) is relevant to gas saturation of equant porosity, whereas the latter situation (equation 4b) clearly applies to water saturation of cracks of low aspect ratio.

The characteristic frequency for local squirt flow between thin cracks, which separates the saturated isolated and saturated isobaric regimes, (O'Connell & Budiansky, 1977; Palmer & Traviolia, 1980) is

$$f_{sq} \cong K_0\alpha^3/2\pi\eta \quad (5)$$

where K_0 is the bulk modulus of the intact medium and α is the crack aspect ratio. For stress-induced fluid flow between cracks and pores, a broadly similar characteristic frequency is expected, because fluid flow within narrow cracks should be rate-controlling in each case.

4.2.3 The Effect of Fluid Saturation on Elastic Moduli Within the Saturated Isolated Regime

It has been demonstrated in Appendix Appendix A how the pore-crack microstructure of the dry cracked medium can be quantified in terms of the concentrations and aspect ratios of both “nonclosable” pores that remain open at P_{max} and also the thin cracks that are subject to pressure-induced closure at pressures $P < P_{max}$. The microstructure thus inferred can be used to predict the elastic moduli of the medium with all of its inclusions (i.e., both cracks and equant pores) fully fluid saturated, at each pressure, using the implicit assumption that fluid is trapped in each inclusion. Additional details on the calculation procedure, based on the model of David and Zimmerman (2012), are given in Appendix Appendix C.

It is recalled that Young's modulus E may be expressed in terms of the bulk and shear moduli as

$$E = 3G/(1 + G/3K). \quad (6)$$

Accordingly, whether or not the shear modulus is increased by fluid saturation, an increase in bulk modulus with fluid saturation results in an increase in Young's modulus.

5 Experimental Results

5.1 Chemical Compositions of the Glass Rod and Glass Bead Materials

Chemical compositions of the soda-lime-silica glasses are reported in Table 1.

Table 1
Chemical Compositions of Glass Rod and Glass Bead Materials

	Weight percent of major oxide components					
Material	SiO_2	Na_2O	CaO	Al_2O_3	K_2O	MgO
Glass rod[a]	79.6 ± 1.5	12.1 ± 4.3	4.9 ± 0.2	1.1 ± 0.1	0.9 ± 0.1	0.0 ± 0.1
Glass beads[b] (300–350 μm)	71.8	12.8	7.7	2.8	0.5	2.3
Glass beads[a] (180–211 μm)	75.4 ± 1.5	10 ± 2	9 ± 3	2.7 ± 1.1	0.6 ± 0.3	0.5 ± 0.6

[a]From electron microprobe energy dispersive X-ray analysis. [b]From scanning electron microscope energy dispersive X-ray analysis.

5.2 Crack Pore Microstructures

The porosities estimated for each specimen through light microscopy (Figure 4), He pycnometry, and mensuration are presented in Table 2. The networks of thermal cracks (Figures 4-6) include cracks of the three preferred orientations, especially type B (containing both longitudinal and radial axes, Figure 4) and type A (normal to the longitudinal axis, Figure 5), interconnected into a three-dimensional network. The low-porosity glass bead specimen A3, fabricated from beads of relatively large diameter (300–350 μm) contains cracks of type B with wide angular separation typically penetrating to the cylinder axis (Figure 4, lower panel). A different pattern is observed for the high-porosity glass bead specimen YF1 (Figure 4, upper panel) fabricated from beads of smaller diameter (180–211 μm) where most of the numerous type B cracks, which nucleated at the cylindrical surface, coalesced and terminated within the outer 40% of the radius. The cracks, introduced into the synthetic glass samples of this study by quenching from 500 °C into water, are of consistently low aspect ratio (Figure 6) like those in thermally cracked borosilicate glass (Ougier-Simonin et al., 2011), and the crack networks are likewise strikingly similar (Mallet et al., 2013, Figure 1). This suits our present purpose because interconnected cracks of low aspect ratio are associated with low permeability—conditions which favor the retention of fluid within the stressed specimen, thereby potentially providing access at appropriate frequencies to the saturated isobaric and saturated isolated fluid flow regimes.

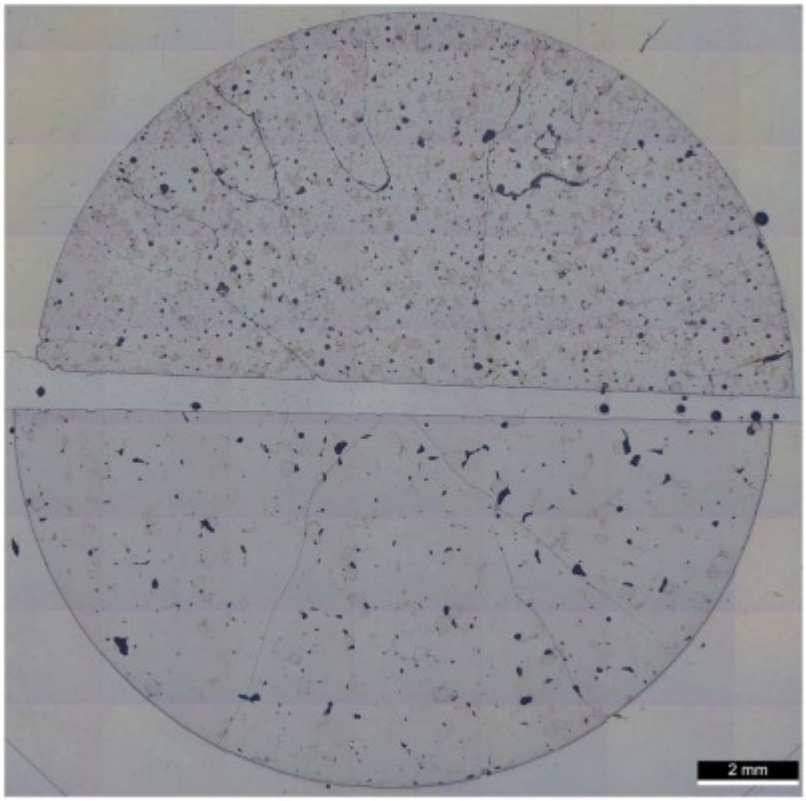

Figure 4

Representative microstructures from mosaic light microscopy on transverse sections of thermally cracked sintered glass bead materials: (upper) high-porosity (~5%) specimen YF1 and (lower) low-porosity (~2%) specimen A3. The porosity, residual after sintering, consists of mainly isolated relatively equant pores (epoxy-filled and dark) located between precursor glass beads delineated by discoloration, presumably associated with oxidized iron impurities. The patterns of dominantly type B cracks are discussed in the text.

Table 2
Characteristics of the Synthetic Glass Materials

Specimen (technique)	L_0 (mm; ±0.001)	D_0 (mm; ±0.001)	ϕ_{cr} (%; ±0.02%)	ϕ_{op} (%)	ϕ_{He} (%)	ρ (kg/m^3)
			Glass rod specimens			
FDSL1(F)	150.010	14.980	0.30	—	—	2,506.24 ± 0.07
FDL1(R)	76.20	38.10	*Intact*	—	—	2,515.58 ± 0.02
FDL2(R)	76.20	38.10	0.74	—	—	2,498.60 ± 0.02
FDL3	76.20	38.10	0.83	—	—	—
FDS2(U)	50.001	15.006	0.35	—	0.5 ± 0.1	2,504.1 ± 0.2
FDS3(U)	49.985	15.008	*Intact*	—	0.3 ± 0.4	2,513.8 ± 0.2
			Low-porosity glass bead specimens			
A3(F*)	49.989	14.992	0.16	2.0 ± 1.0	—	—
A4(F*)	49.995	14.994	0.20	2.0 ± 0.7	1.0 ± 0.1	2,447 ± 1
A5(F*U)	50.009	14.996	0.08	1.8 ± 0.7	0.5 ± 0.1	2,448 ± 1
Y2(U)	49.984	14.971	*Intact*	3.2 ± 1.5	0.1 ± 0.1	2,440 ± 1
Y4	49.969	14.966	0.29	3.0 ± 1.3	0.9	2,447 ± 1
			High-porosity glass bead specimens			
YF1(F*U)	49.965	14.991	0.14	5.4 ± 1.5	2.5 ± 0.2	2414.2 ± 0.2
YF2(F*)	49.971	14.991	0.22	6.0 ± 0.8	3.4 ± 0.1	2410.0 ± 0.2
YF3(F*)	49.984	14.996	0.28	5.9 ± 0.8	2.9 ± 0.1	2410.9 ± 0.2
YF4(U)	49.995	15.001	Intact	4.6 ± 1.2	0.6 ± 0.2	2426.7 ± 0.2

Note. Measurement techniques: forced oscillation (F), forced oscillation on a stack of three specimens (F*), resonant bar (R), ultrasonic (U); L_0: sample length before cracking; D_0: sample diameter before cracking; ϕ_{cr}: crack porosity calculated as the dimensional change of a cylindrical sample after thermal cracking; ϕ_{op}: total equant porosity determined by optical microscopy; ϕ_{He}: connected porosity determined by helium pycnometry; ρ: bulk density of dry sample.

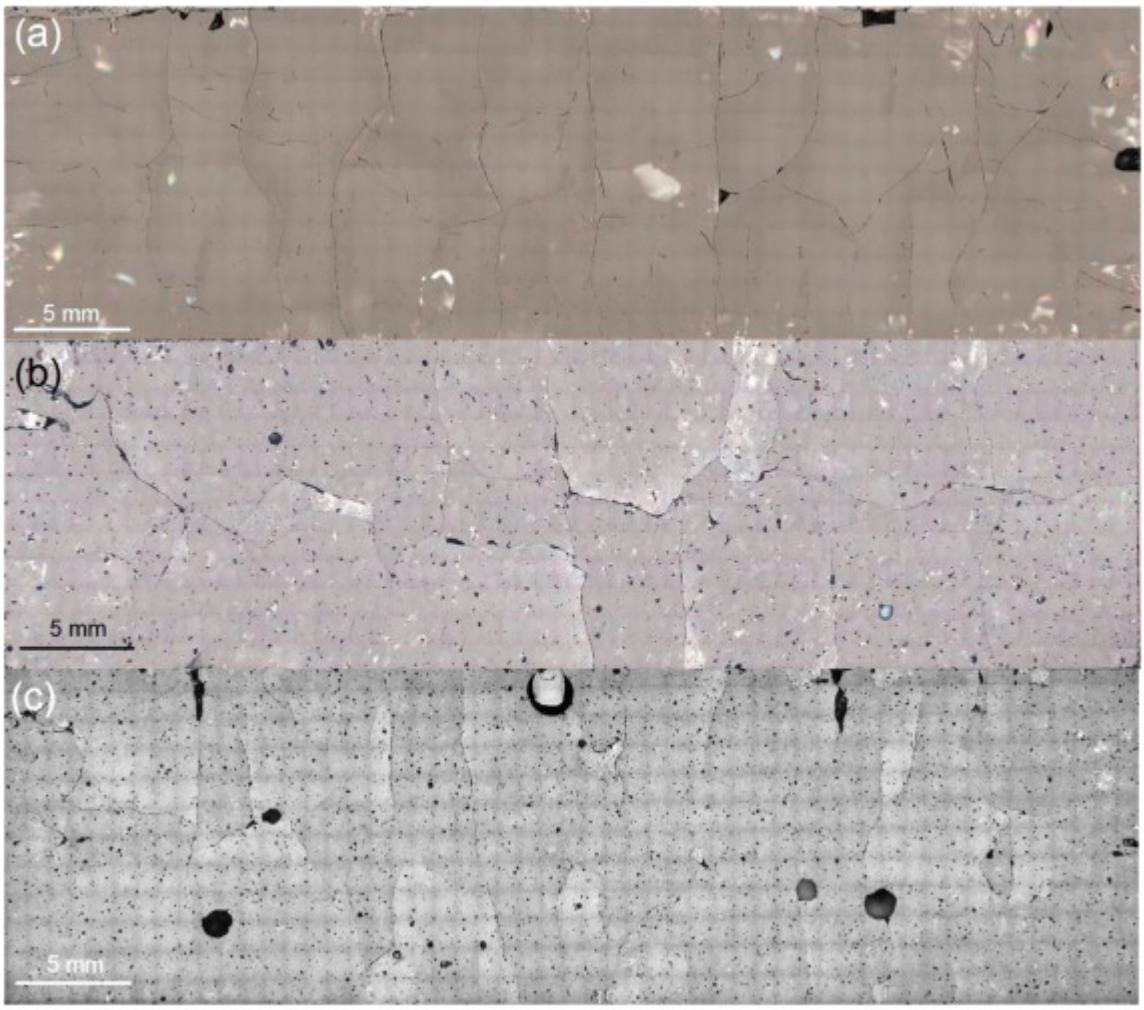

Figure 5

Crack networks visible in central longitudinal cross sections (of 50 mm length and 15 mm diameter) of (a) glass rod specimen (FDS2); (b) low-porosity glass bead specimen (A3); (c) high-porosity glass bead specimen (YF1). Numerous type A cracks, oriented approximately normal to the cylinder axis, are linked by cracks oriented more nearly parallel with the cylinder axis. Dark areas are mainly epoxy-filled pores along with some voids, especially in panel (a), created by plucking of glass fragments during preparation of the section.

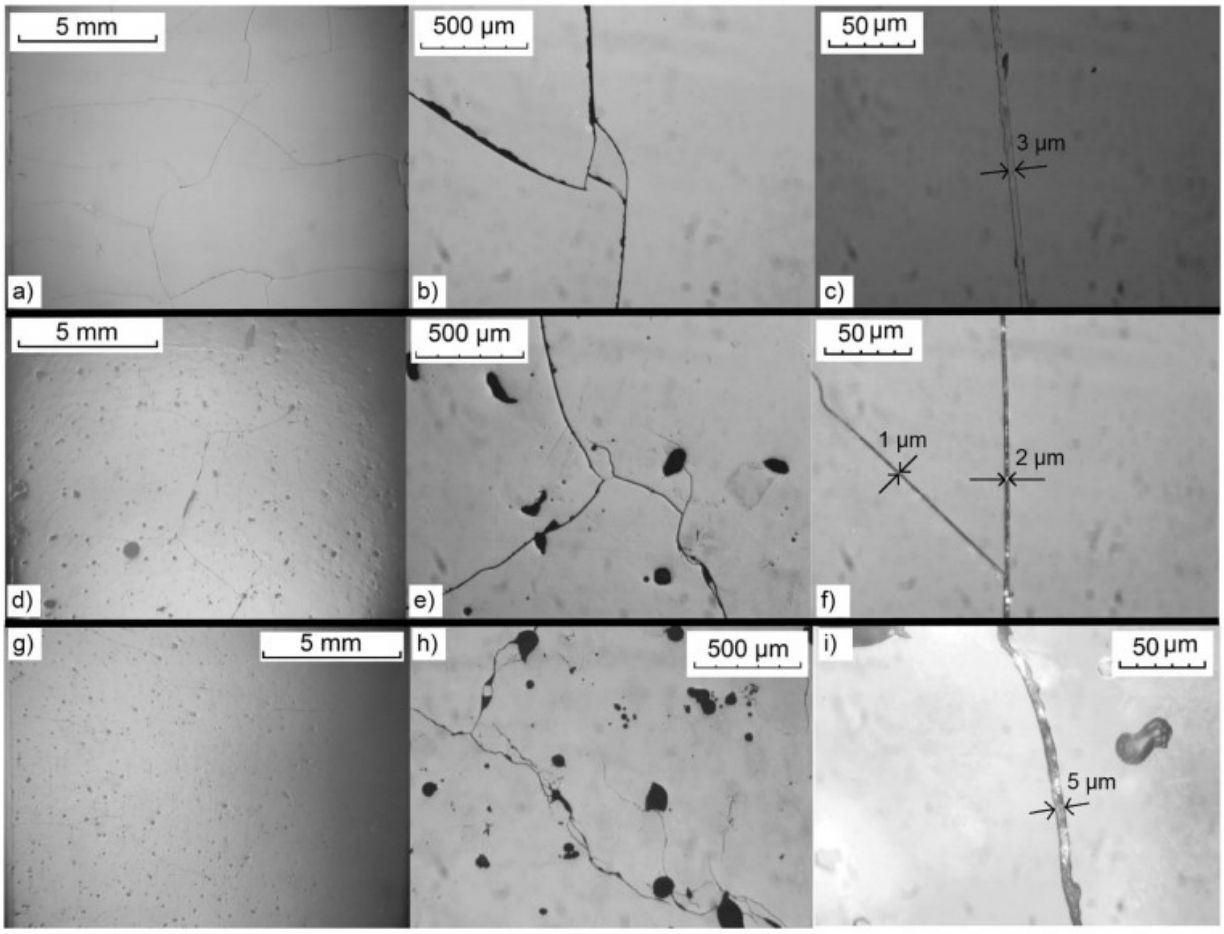

Figure 6

Crack network in (a–c) glass rod specimen (FDS2), (d–f) low-porosity glass bead specimen (A3), (g–i) high-porosity glass bead specimen (YF1), imaged by light microscopy with progressively increasing magnification for each specimen from left to right. Images were taken on a longitudinal cross section for each specimen (see Figure 5).

The sintered glass bead specimens, whether of ~2 or ~5% equant porosity, have similar optically estimated averaged crack aspect ratios ~ 10^{-3} (cf. 7×10^{-4}, Olin, 2011, for similarly prepared material). However, the cracked glass rod specimens have cracks of systematically larger aperture and hence crack porosities and aspect ratios 2–3 times larger than those of the glass bead specimens. That the measured crack density and mean aspect ratio are largest for the cracked glass rod specimen of larger diameter tested with the resonant bar technique (Table 3) suggests that the crack distributions may vary with the dimensions of the glass specimens. Concerning the reliability of measured crack aspect ratios, Delle Piane et al. (2015) found that aspect ratios for cracks in thermally treated Carrara marble determined from two-dimensional sections imaged by SEM are larger than those inferred from 3-dimensional micro-CT. It is conceded that crack aspect ratios are very difficult to measure precisely and therefore that the estimates in Table 3 are only indicative. A more reliable alternative method for evaluating crack

aspect ratios is provided by the pressure dependence of elastic moduli, as discussed below.

Table 3
Characteristics of the Populations of Thermal Cracks

Sample	Sample name	Crack network	Mean crack length (mm)	Mean crack aperture (μm)	Mean aspect ratio	Crack porosity (%; ± 0.02%)	Crack density
Small-dimension glass rod specimen	FDS2	Types A, B, and C, dominated by long cracks	3.9	7.5	0.002	0.35	0.4
Large-dimension glass rod specimen	FDL3	Types A, B, and C, both long and short cracks	6.4	21.3	0.003	0.83	0.7
Small-dimension low-porosity glass bead specimen	A3	Types A, B, and C, dominated by long cracks	4.6	4.4	0.001	0.16	0.4
Small-dimension high-porosity glass bead specimen	YF1	Types A, B, and C, both long and short cracks	4.6	4.4	0.001	0.14	0.3

Additional information concerning crack porosity and pressure-induced crack closure is provided by in situ CT scanning conducted in conjunction with the resonant bar measurements on cracked glass rod specimen FDL2. The contrasting X-ray absorption measured at atmospheric pressure (Figure 7a) and on the same material at 25 MPa indicates an average closable porosity of ~0.14% (Figure 7b)—an only modest fraction of the total crack porosity (0.74%) determined on the same specimen by mensuration (Table 2).

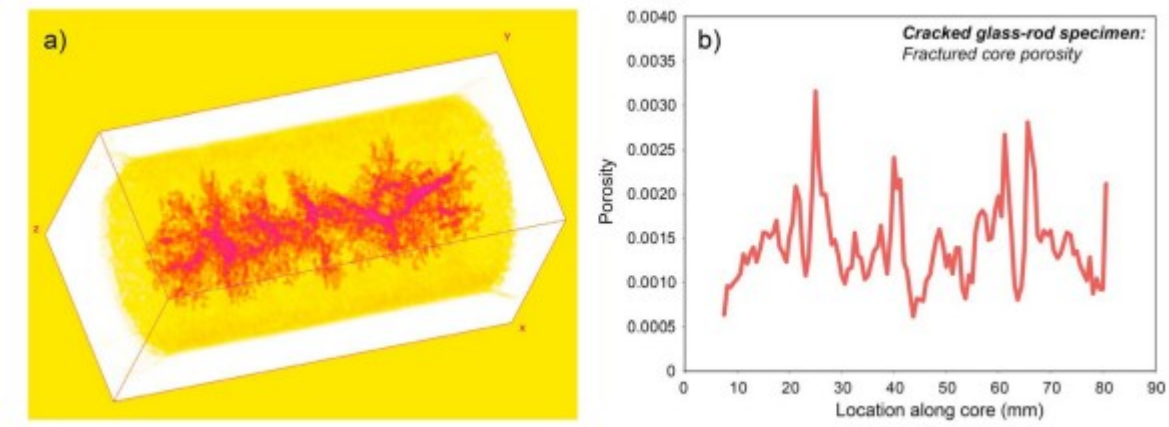

Figure 7

(a) A computed tomography image obtained at atmospheric pressure of cracked glass rod specimen FDL2 showing the largest fractures that are concentrated toward the axis of the cylindrical specimen with branches extending to the surface. (b) The crack porosity inferred by comparison of computed tomography data obtained on the same specimen at atmospheric pressure and at a confining pressure of 25 MPa—computed for circular slices of 0.625 mm thickness perpendicular to the cylinder axis.

5.3 Permeability

The argon permeability, measured by transient flow, for each of the three types of specimen is presented as a function of differential pressure P_d (confining pressure − pore pressure) in Figure 8. A generally systematic trend of decreasing permeability with increasing differential pressure is noted for each sample. The rate of decrease in permeability with increasing differential pressure decreases systematically with increasing differential pressure. The permeabilities of the three samples are similar at

differential pressures ~10 MPa but diverge at higher differential pressures where the permeability of the high-porosity glass bead sample is systematically higher than that of the low-porosity glass bead sample, and the glass rod specimen, in turn. For the glass rod specimen with P_d ~ 100 MPa, it proved impossible to attain pore pressure equilibrium between the upper and lower reservoirs, thereby defining a threshold ~5×10^{-20} m^2 below which permeability could not be reliably measured. Uncertainty arises from two sources: (1) the variation during equilibration of pore fluid properties, for example, argon bulk modulus and viscosity, relative to average values used in the calculation of k; and (2) uncertainty in rate constant A associated with specification of the time interval over which the evolution of pore pressure in the upstream reservoir is to be fitted.

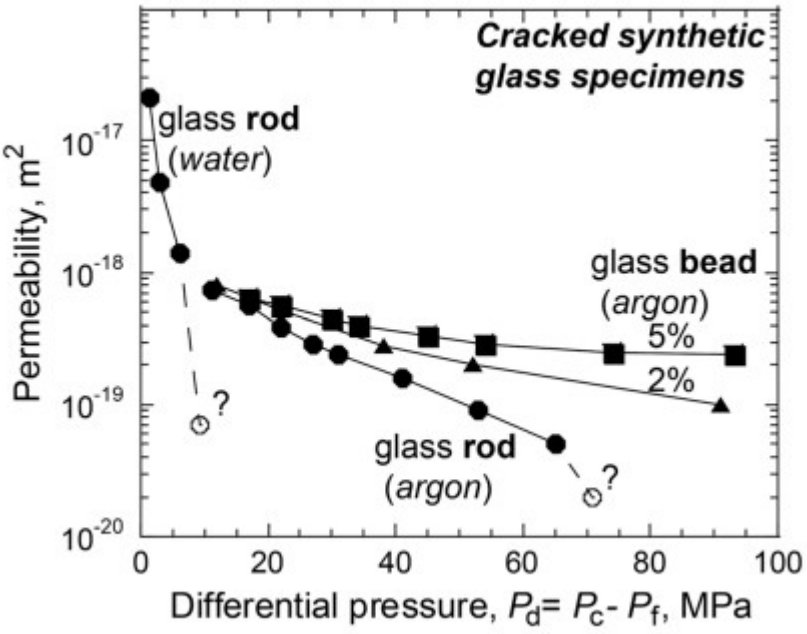

Figure 8

Argon permeability measured as a function of differential pressure by the transient flow method on thermally cracked specimens of each of the three synthetic glass media: glass rod specimen (circles), low-porosity (~2%) glass bead specimen (triangles), and high-porosity (~5%) glass bead specimen (squares), along with water permeability measured on a glass rod specimen of larger dimension by the steady state flow method.

The permeability of the glass rod specimen, measured with tap water as pore fluid by steady state flow, decreases by 3 orders of magnitude from 2×10^{-17} m^2 at the lowest differential pressure of 1.3 MPa to 7×10^{-20} m^2 at the highest differential pressure of 9.3 MPa (Figure 8). Uncertainties are associated with location of the water front within the rubber tubing and slight variations in temperature (±2 °C) which perturb the viscosity of water by up to 5%. The overall uncertainty of water permeability, therefore, is estimated to be ~10%.

5.4 Strain Measurements

The strain data obtained in conjunction with the ultrasonic wave speed measurements indicate axial and circumferential strains of 0.07–0.09% over the pressure range of 10 to 100 MPa for both cracked and intact specimens (Figure 9). For the cracked specimens, there is an additional strain of 0.03–0.06% below 10 MPa in the axial direction, but no such low-pressure contribution to the total strain measured circumferentially on the cracked glass rod specimen. Both axial and circumferential strains are of order 0.1% at the highest confining pressure of 100 MPa for all synthetic samples. The effect of confining pressure on the strain gages was neglected as this as has been shown to be small (~10^{-6}) using fused quartz standards (Bakhorji, 2010).

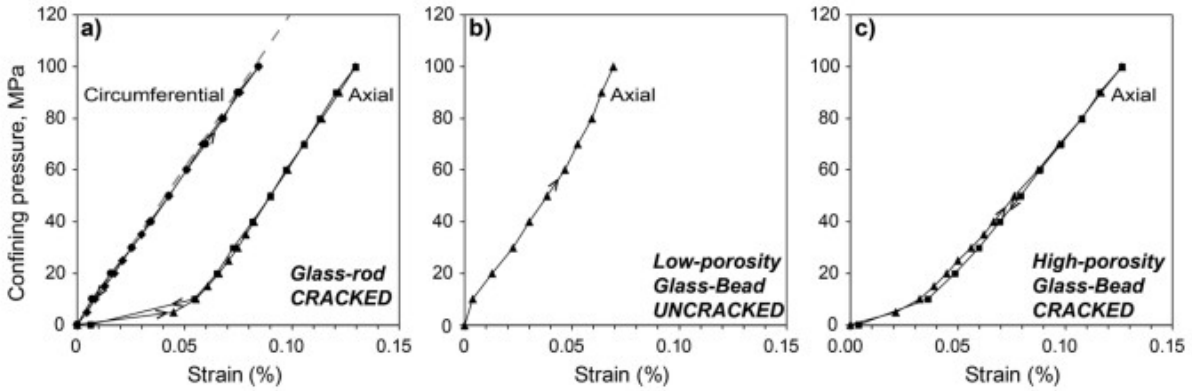

Figure 9

(a) The pressure dependence of the axial and circumferential strains for a cracked glass rod specimen, compared with the elastic strain expected for a bulk modulus of 40 GPa (dashed grey line); (b) the axial strain for an uncracked low-porosity glass bead specimen; and (c) the axial strain for a cracked high-porosity glass bead specimen. Arrows along curves indicate pressure path during the experiment.

5.5 Dissipation and Dispersion at Millihertz-Hertz Frequencies

The strain-energy dissipation Q^{-1} measured in torsional forced oscillation at millihertz-hertz frequencies on the glass specimens is consistently low (<0.005) and decreases systematically with increasing pressure below 30 MPa to values generally <0.002 at higher pressures. However, the low-porosity glass bead specimen displays higher levels of dissipation than the other two specimens, and distinctively, a systematic frequency dependence whereby Q^{-1}increases with decreasing frequency to values as high as 0.005 at 0.01 Hz and P = 10 MPa (Figure 10). Such dependence of dissipation Q^{-1} upon angular frequency ω and the associated dispersion of the shear modulus $G(\omega)$ are best expressed, internally consistently, in terms of the real $J_1(\omega)$ and negative imaginary $J_2(\omega)$ parts of the complex compliance $J^*(\omega)$ that is essentially the Laplace transform of an appropriate creep-function $J(t)$ (e.g., Jackson, 2015):

$$G(\omega) = \left[J_1^2(\omega) + J_2^2(\omega)\right]^{-1/2} \text{ and } Q^{-1} = J_2(\omega)/J_1(\omega). \quad (7)$$

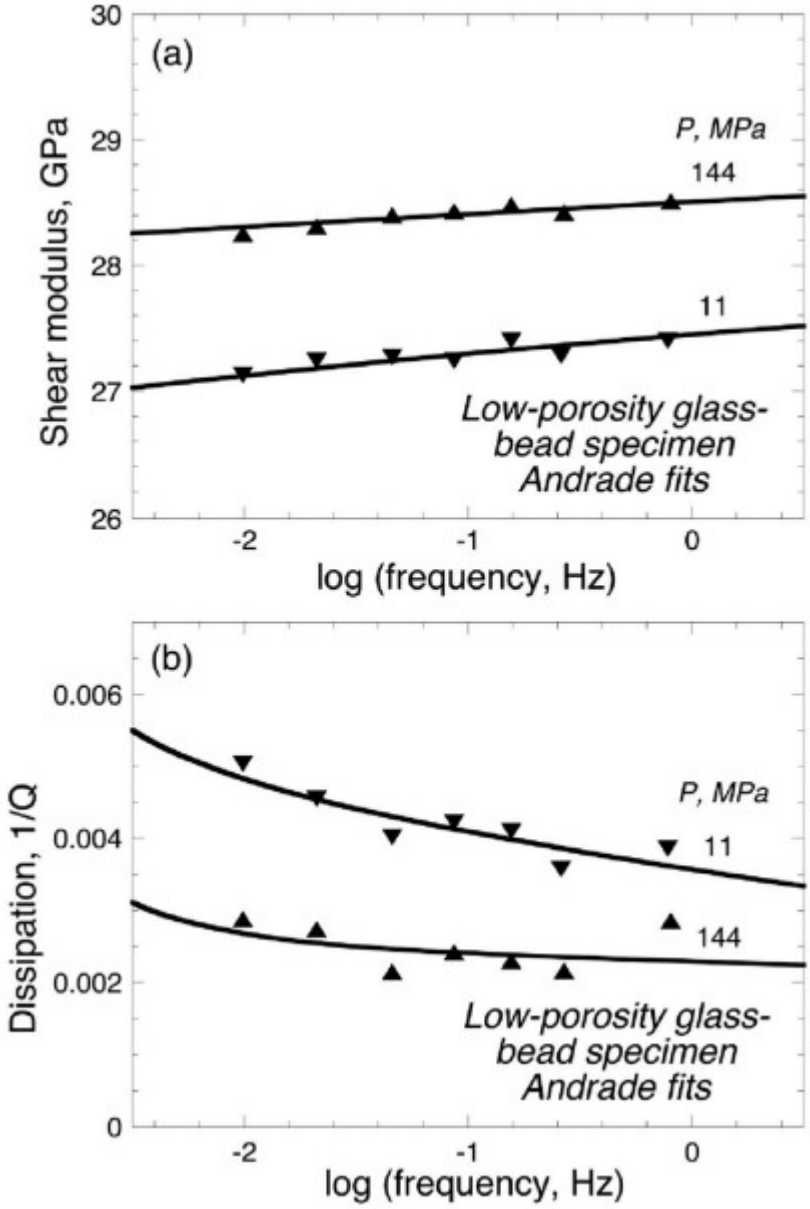

Figure 10

(a) Shear modulus dispersion and (b) associated strain energy dissipation, for the low-porosity glass bead specimen subjected to torsional oscillation tests under dry conditions at representative pressures of 11 and 144 MPa in torsional oscillation. Each curve represents the Andrade model least squares fitted to both modulus and dissipation data.

For the fitting of the representative modulus and dissipation data of Figure 10 for the low-porosity glass bead specimen, an Andrade creep function, of the form

$$J(t) = J_U + \beta t^n + t/\eta, \qquad (8)$$

was employed. The first, second, and third terms on the right-hand side of equation 8represent, respectively, the instantaneous elastic response given by the unrelaxed compliance J_U, the recoverable (anelastic) strain specified as coefficient β times the nth power of time t, and a permanent strain inversely proportional to the viscosity η.

The shear moduli inferred from forced oscillation measurements for the glass specimens are thus at most mildly, and similarly, frequency dependent. The most robust data for oscillation frequencies logarithmically equally spaced between 0.01 and 0.26 Hz are accordingly averaged for the following analyses of the variation of moduli with confining pressure P_c and/or differential pressure $P_d = P_c - P_f$.

5.6 Mechanical Properties: Cracked Glass Rod Material

5.6.1 Forced-Oscillation Measurements at Millihertz-Hertz Frequencies

For the initial measurements on cracked specimen FDSL1 under dry conditions, the period-averaged shear modulus increases substantially with increasing confining pressure to ~30 MPa, thereafter remaining essentially constant for the pressure interval 30–70 MPa, and decreasing slightly with further increase of pressure to 100 MPa (Figure 11a). Preliminary examination of the data obtained under conditions of fluid saturation confirmed that variations of modulus with P_c and P_f are adequately expressed in terms of the differential pressure alone. With argon saturation, the shear moduli are broadly consistent with the dry values—no systematic increase in modulus (i.e., stiffening) being observed for either cycle of differential pressure variation. The first such cycle involved increasing differential pressure achieved by decreasing pore pressure P_f with P_c held constant near 100 MPa. Subsequently, the differential pressure was progressively decreased by reducing P_c with P_f constant at 10 MPa, with evidence of some hysteresis between the two cycles. In the dry measurement repeated following argon saturation, the trend of dry shear moduli with pressure is generally consistent with that observed in the initial dry measurement, although the shear moduli tend to be slightly higher in the repeat experiment.

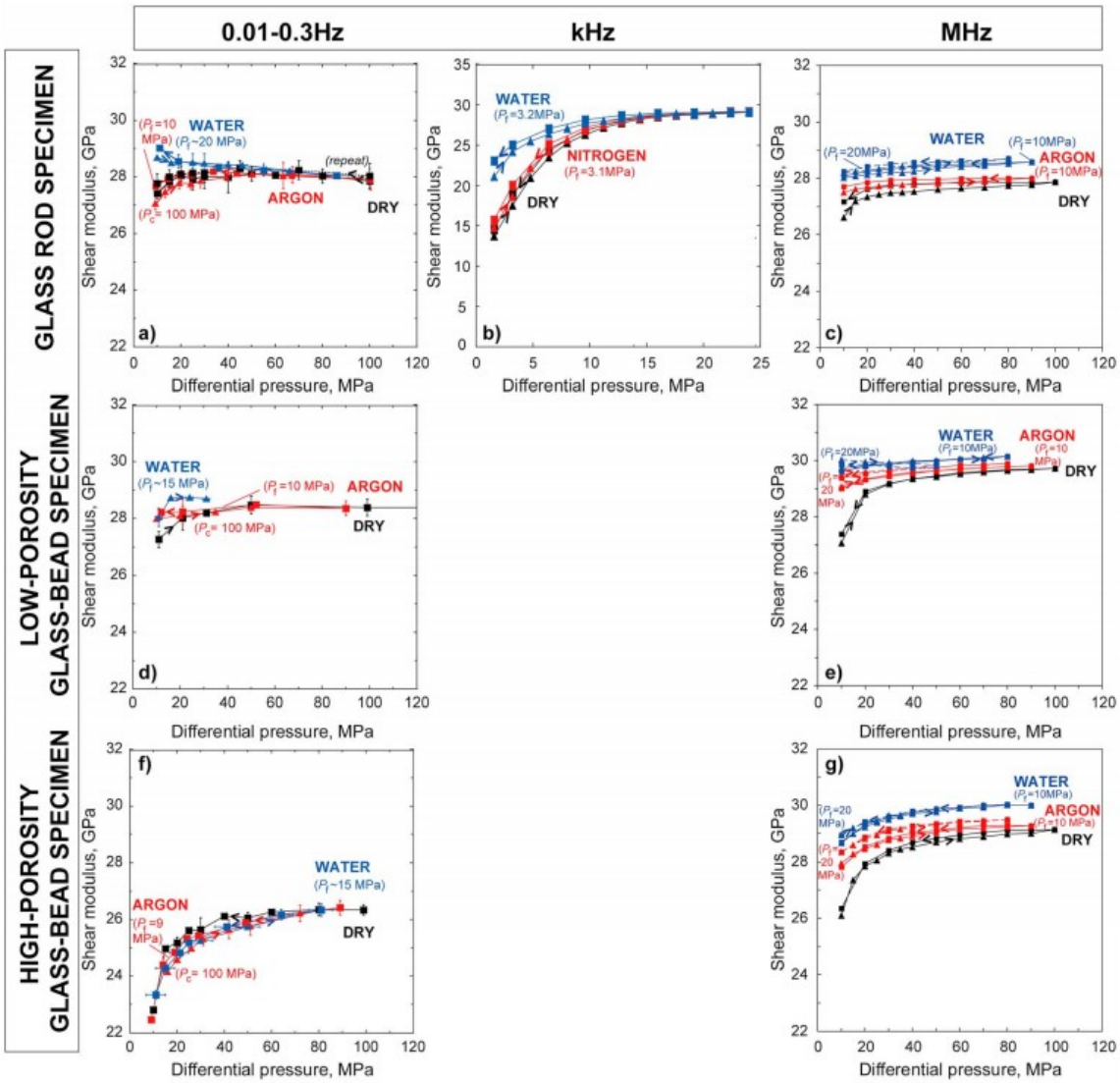

Figure 11

A summary of the broadband (0.01–0.3 Hz, kHz, and MHz) shear modulus data for the suite of thermally cracked synthetic glass media. The data derive from forced oscillation (period-averaged values are plotted), resonance bar, and ultrasonic wave propagation tests on glass rod specimens and on glass bead specimens of low (~2%) and high (5%) porosity. The error bars for the moduli measured by forced oscillation reflect uncertainties inherent in the conversion of measured AC bridge voltages into displacements. The error bars for differential pressure, significant only for water saturation, reflect potentially incomplete pore pressure equilibration under conditions of low effective permeability. The variations of shear modulus are plotted on a common scale for ease of comparison, except for the glass rod specimen tested at kilohertz frequencies, where a wider variation in modulus is observed across a narrower range of differential pressure.

With water saturation, the pattern is one of systematically higher shear moduli, that is, stiffening, for P_d < 40 MPa, with a maximum increase of 5% from the dry value at ~10 MPa (Figure 11a). Beyond ~40 MPa, the shear moduli with water saturation approach the moduli measured under dry and argon-saturated conditions. The “water-saturated” shear moduli measured in the increasing and decreasing differential pressure cycles are generally

consistent, although minor hysteresis at the lowest pressures may reflect a degree of pore pressure disequilibrium between specimen and the external reservoirs. A mild decrease in shear modulus with increasing pressure, similar to that observed in dry measurements beyond 50 MPa, is also noticed with water saturation.

5.6.2 Resonant Bar Measurements at 1- to 2-kHz Frequency

Resonant bar experiments have been conducted on both intact (FDL1) and cracked (FDL2) glass rod specimens. For the intact specimen, both shear and Young's moduli exhibit pressure sensitivity for pressures below a threshold near 10 MPa, beyond which the moduli become essentially pressure independent (Figure 12).

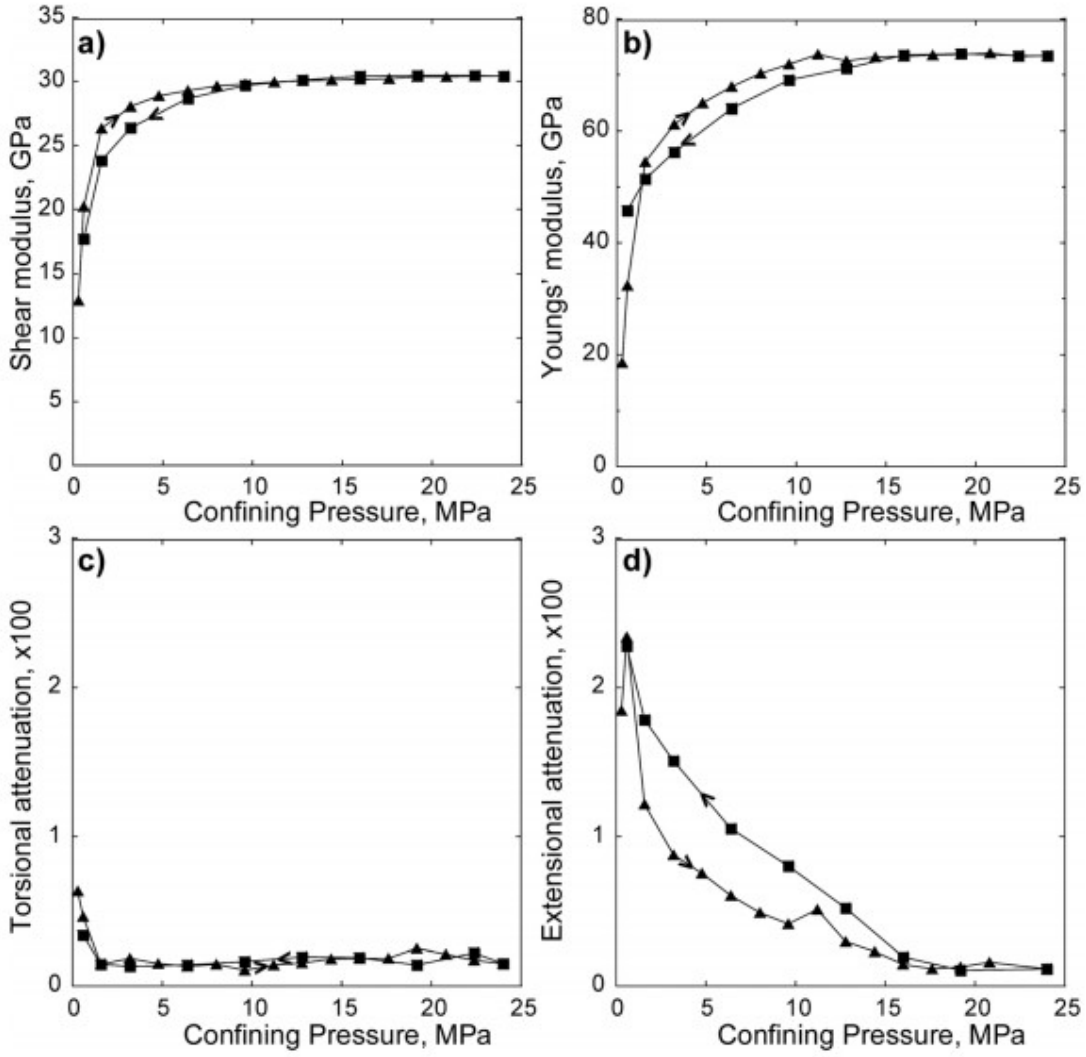

Figure 12

Mechanical properties of an intact glass rod specimen (FDL1) measured dry at kilohertz frequencies: (a) shear modulus (±1%) and (c) associated torsional attenuation $1/2Q_G$ at 1.2–1.5 kHz; (b) Young's

modulus (±1%) and (d) associated extensional attenuation $1/2Q_E$ at 1.7–2.4 kHz. Arrows along curves indicate pressure path during the experiment.

The transition between the pressure-dependent modulus at low confining stress and the approximately constant modulus beyond the pressure threshold for the intact specimen is attributed to diminishing compliance associated with the coupling between the specimen and end-pieces. We determined the value of such pressure-dependent interfacial compliance for the cracked specimen from the data for the intact specimen, based upon the reasonable assumption that in the absence of the interfacial effect, the intact specimen should exhibit a pressure-independent modulus equal to that determined by the resonant bar technique at the highest pressure. The interfacial compliances related to the shear and Young's moduli are subtracted from the measurements conducted at the same differential pressure on the cracked specimen (Figures 13a and 13b), to yield “interface-adjusted” shear and Young's moduli (Figures 13c and 13d, reproduced in the summary Figures 11b and 14a).

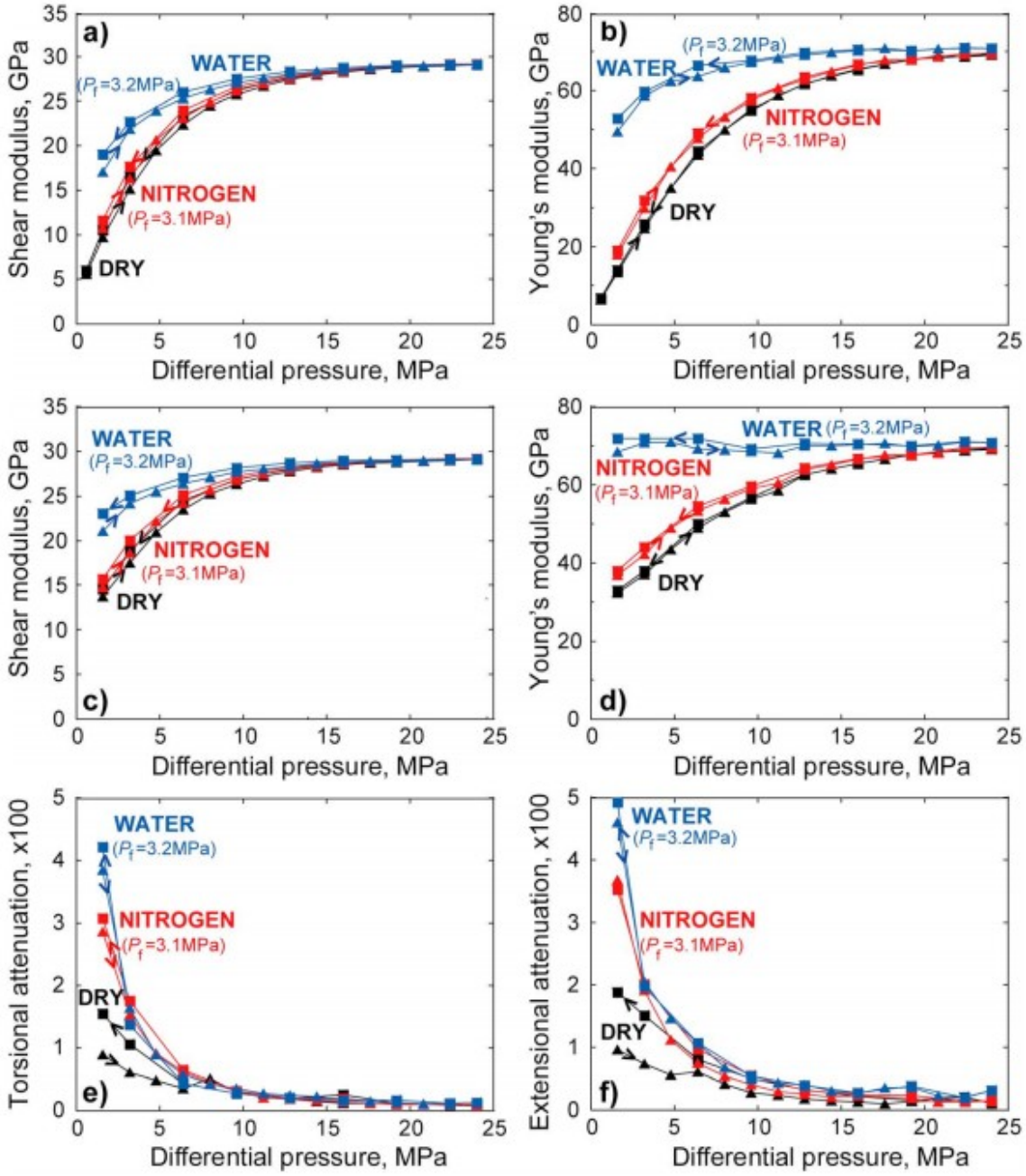

Figure 13

Results of resonant bar experiments on the cracked glass rod specimen FDL2, conducted at resonance frequencies of 1.1–1.5 kHz (torsional mode) and 1.5–2.4 kHz (extensional mode), under dry, nitrogen-saturated, and water-saturated conditions in sequence. (a) Shear modulus, (b) Young's modulus, (c) shear modulus adjusted for interfacial compliance as explained in the text, (d) Young's modulus adjusted for interfacial compliance as explained in the text, (e) torsional, and (f) extensional mode attenuation uncorrected for any interfacial contribution. The uncertainty of modulus is ±1%. Arrows along curves indicate pressure path during the experiment.

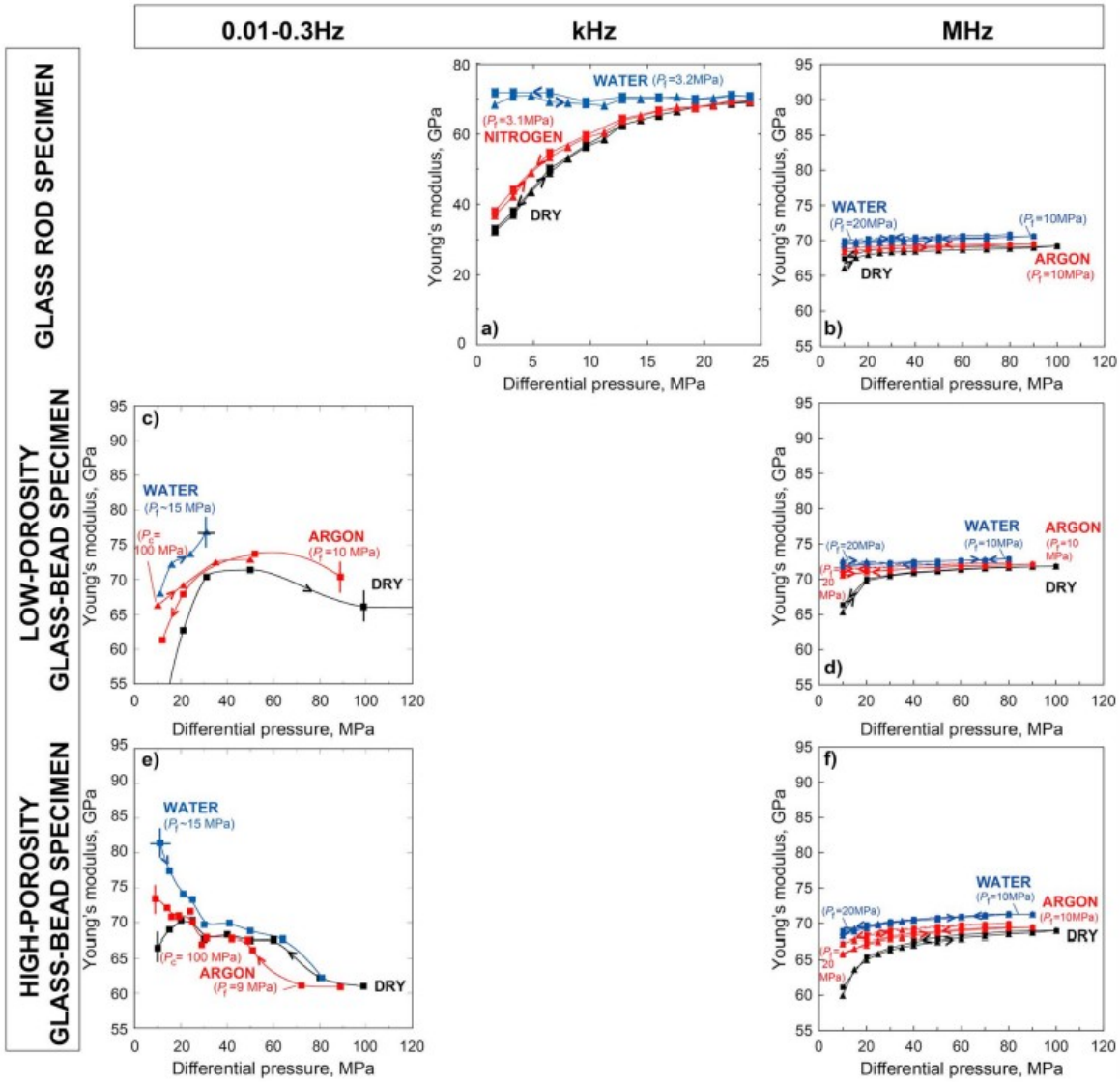

Figure 14

A summary of the broadband (0.01–0.3 Hz, kHz, and MHz) measurements of Young's modulus for the suite of cracked synthetic glass media. The data derive from forced oscillation (where period-averaged moduli are plotted), resonance bar, and ultrasonic wave propagation tests on glass rod specimens, and on glass bead specimens of low and high porosity. The representative error bars (±2 GPa) for Young's modulus include contributions from uncertainties in the calibration of the displacement transducers, and from approximations in the finite difference modeling of flexural oscillation. The error bars for differential pressure have the same significance as in Figure 11. The variations of Young's modulus are plotted on a common scale for ease of comparison, except for the glass rod specimen at kilohertz frequency, where a wider variation in modulus is observed across a narrower range of differential pressure.

Generally, the interface-adjusted shear modulus for the cracked specimen increases with increasing pressure below 15 MPa, thereafter becoming essentially pressure independent. Modest stiffening is observed with nitrogen saturation. Due to minor hysteresis during pressure cycling (thought to be caused by the elastoplastic deformation of the metal foils at the interfaces),

the nitrogen-saturated shear modulus is compared with the dry modulus in the same pressure cycle, that is, either increasing or decreasing differential pressure. The nitrogen-saturated shear modulus converges with the dry modulus at higher pressures of 10–15 MPa. In contrast, the water-saturated modulus shows smaller but still substantial increases at pressures below 15 MPa and again converges with the dry modulus at pressures beyond 15 MPa. For shear attenuation, relatively high values are observed below 10 MPa (Figure 13e). The shear attenuation with water saturation is systematically higher than that with nitrogen saturation, and in turn higher than the dry attenuation.

The interface-adjusted Young's modulus *E* also increases markedly with increasing pressure under both dry and nitrogen-saturated conditions. In contrast to the shear modulus behavior, however, for water-saturated conditions, *E* is almost independent of pressure for the entire pressure range. At the lowest differential pressure of 1.6 MPa, nitrogen saturation increases *E*by ~15% from 33 GPa, whereas water saturation roughly doubles the Young's modulus to ~70 GPa. The extensional attenuation shows relatively high values below 10 MPa (Figure 13f).

The attenuation with water saturation systematically shows higher values than that with nitrogen saturation, which in turn is higher than the values under dry conditions. Beyond 10 MPa, the extensional attenuation shows consistently low values of 0.001–0.005 under all conditions. Both shear and extensional attenuation measured on the dry cracked material (Figures 13e and 13f) are similar to those for the intact specimen (Figures 12c and 12d), which suggests some contribution from the interfacial effects.

5.6.3 Ultrasonic Measurements at 1-MHz Frequency

Ultrasonic measurements have been performed on both intact and cracked glass rod specimens. For the intact glass rod specimen FDS3, the shear modulus and Young's modulus are generally pressure independent, with values of 31 GPa and 75 GPa, respectively, except for a minor pressure dependence observed below 20 MPa (Figures 15a and 15c). The moduli measured during depressurization match those obtained during pressurization well. The shear and Young's moduli for the dry cracked glass rod specimen FDS2 increase markedly with increasing pressure below 20 MPa (Figures 15b and 15d and also 11c and 14b). *G* and *E*increase more mildly with increasing pressure beyond 20 MPa, and at 100 MPa remain significantly lower than for the intact specimen by ~10 and ~8%, respectively. Such large modulus deficits stand in marked contrast to results obtained on another glass rod specimen FDS1 prior to the development of a throughgoing fracture, and deficits of only 0–2% for the glass bead specimens. For argon saturation, the shear and Young's moduli are systematically higher than the dry moduli at pressures below 20 MPa, and gradually approach the dry moduli with increasing differential pressure.

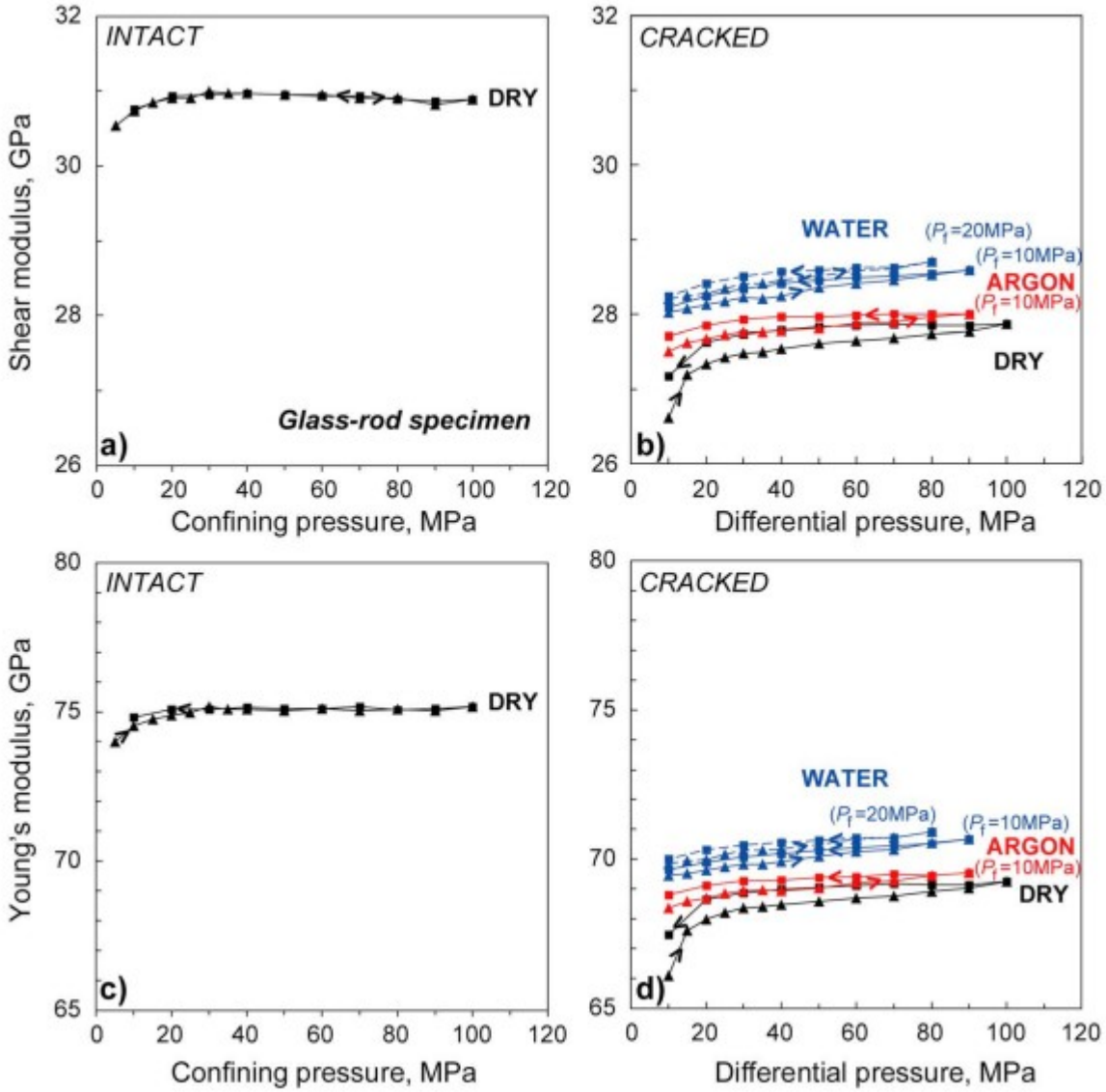

Figure 15

The results of ultrasonic measurements at 1-MHz frequency for glass rod specimens. (a) Shear and (c) Young's moduli for a dry intact glass rod specimen FDS3; (b) shear and (d) Young's moduli of a cracked glass rod specimen FDS2 obtained under dry, argon- and water-saturated conditions. The uncertainty associated with the determined moduli is about ±1%. Arrows along curves indicate pressure path during the experiment.

With water saturation, the shear and Young's moduli become even higher than those with argon saturation, and the moduli measured with 20 MPa pore pressure are slightly higher than those with 10 MPa pore pressure at the same differential pressure. The strong pressure sensitivity, observed below 20 MPa under dry conditions, is absent under fluid-saturated conditions.

5.7 Mechanical Properties: Low-Porosity Glass Bead Specimens

5.7.1 Forced-Oscillation Tests at Millihertz-Hertz Frequencies

A compound low-porosity (~2%) glass bead specimen, comprising a stack of three separate cylinders A3, A4, and A5 (Table 2), was tested in both torsional and flexural modes to yield shear and Young's moduli, respectively —successively under dry, argon-saturated, and water-saturated conditions. As for the glass rod specimen, the shear moduli measured at frequencies between 0.01 and 0.26 Hz, at a given pressure, are averaged and plotted against confining or differential pressure (Figure 11d). For dry conditions, the shear modulus increases significantly with increasing pressure below 50 MPa and levels off beyond this pressure threshold. With argon saturation, the shear moduli are systematically higher than the dry moduli by as much as 3% at P_d ~10 MPa. Significant hysteresis is observed between the increasing and decreasing differential pressure cycles. Under water-saturated conditions, the shear modulus at the lowest differential pressure of ~10 MPa is comparable with that observed for argon saturation, whereas a markedly larger value of shear modulus (~28.7 GPa) is observed for higher values of P_d ranging between 16 and 31 MPa.

The Young's modulus under dry conditions increases markedly with increasing pressure to 50 MPa, thereafter decreasing somewhat with increasing pressure (Figure 14c). For argon saturation, significant stiffening is observed below 30 MPa; at higher pressures, the Young's modulus is modestly higher than the dry value. For water saturation, the Young's modulus is systematically significantly higher than for dry and argon-saturated conditions. For both argon- and water-saturated conditions, diminishing interfacial compliance may contribute to the strongly increasing Young's modulus with increasing P_d.

5.7.2 Ultrasonic Measurements at Megahertz Frequency

The elastic moduli for the intact low-porosity glass bead specimen Y2 (Figures 16a and 16c) are systematically lower than those of the intact glass rod specimen (Figures 15a and 15c), clearly illustrating the influence of porosity. The shear and Young's moduli of the intact low-porosity glass bead specimen show mildly increasing trends with increasing confining pressure. Comparison of data in Figure 16c obtained while increasing and decreasing pressure reveals minor hysteresis for the Young's modulus, but no such hysteresis for the shear modulus.

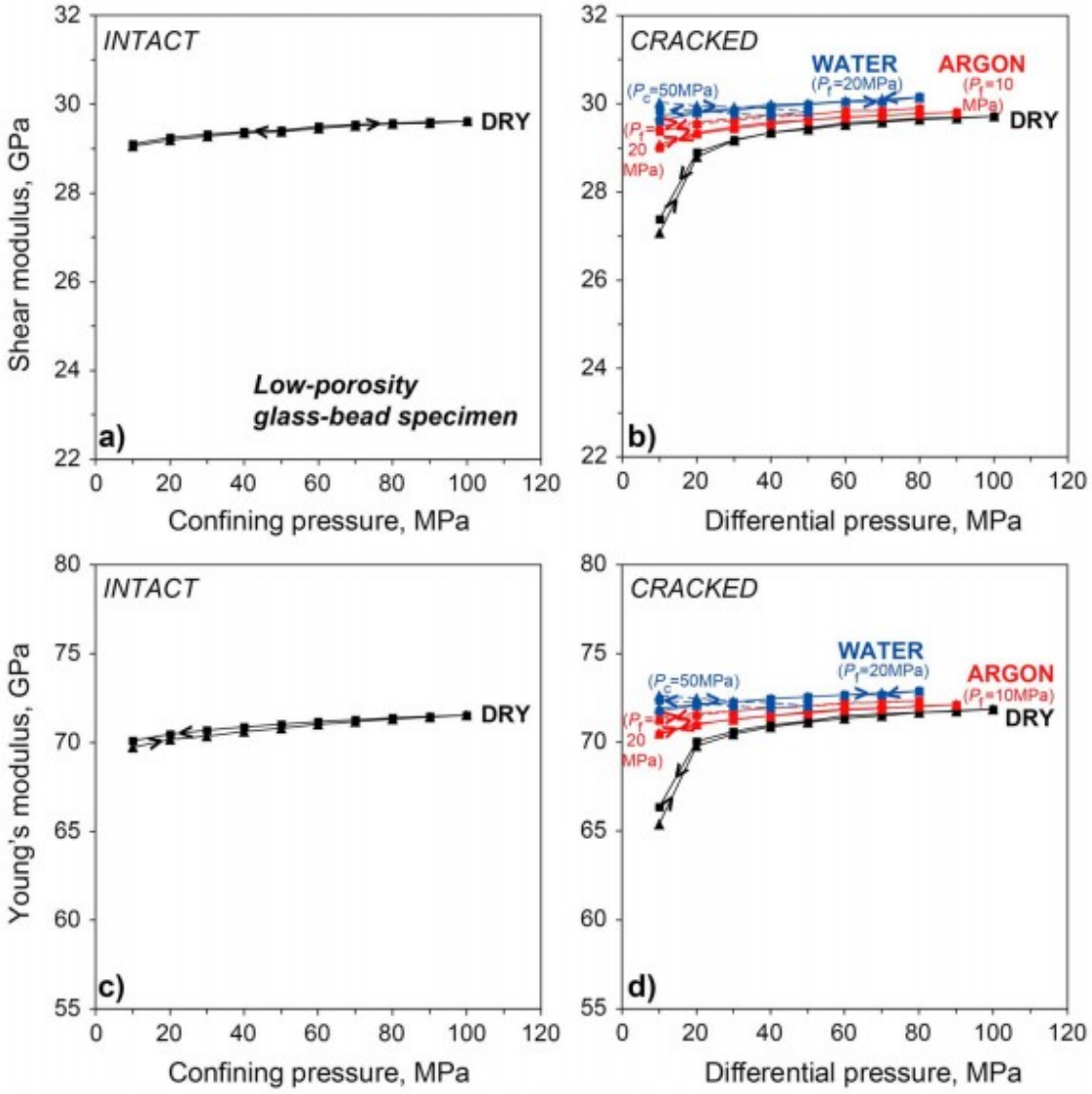

Figure 16

The dry (a) shear and (c) Young's moduli of an intact low-porosity glass bead specimen (Y2). The (b) shear and (d) Young's moduli of a cracked low-porosity glass bead specimen (A5) under dry, argon- and water-saturated conditions. The uncertainty associated with the determined moduli is about ±1%. Arrows along curves indicate pressure path during the experiment.

For the cracked specimen A5, the dry shear and Young's moduli increase significantly with pressure between 10 and 40 MPa, thereafter increasing only slightly to 100 MPa (Figures 16b and 11e, and 16d and 14d, respectively). With argon saturation, the pore fluid pressure was initially maintained at 10 MPa, and a series of differential pressures was achieved by varying the confining pressure. Under such conditions, the shear and Young's moduli are markedly higher than the dry moduli at pressures below 50 MPa and converge toward the dry moduli from 50 to 100 MPa. During the second stage of argon saturation, P_f was fixed at 20 MPa. The resultant shear and

Young's moduli are systematically ~1% higher than the values measured with P_f = 10 MPa at the same differential pressure. With water saturation, P_f was maintained at 20 MPa during the first stage of measurements, and P_c was varied to cover the desired range of increasing and then decreasing differential pressure. During a second series of tests under water-saturated conditions, the confining pressure was maintained at 50 MPa, with P_f varied to achieve differential pressures from 10 to 50 MPa. The shear and Young's moduli are generally systematically higher for water saturation than those measured with argon saturation (Figure 16).

5.8 Mechanical Properties: High-Porosity Glass Bead Specimens

5.8.1 Forced Oscillation Tests at Millihertz-Hertz Frequencies

The shear moduli determined in torsional forced oscillation, averaged between 0.01 and 0.26 Hz, on a cracked composite glass bead specimen of high porosity (comprising a stack of the three cylinders YF1, YF2, and YF3 of Table 2) are displayed as a function of confining/differential pressure in Figure 11f. For dry conditions, the shear modulus increases markedly with increasing pressure below ~40 MPa, thereafter varying more mildly with pressure. With fluid saturation, either argon or water, there is certainly no systematic increase of the shear modulus relative to dry conditions; indeed, the “fluid-saturated” moduli tend to be somewhat lower than those for dry conditions. There is a hint of hysteresis amongst the data for argon saturation.

Under dry conditions, the Young's modulus increases with pressure below 25 MPa (Figure 14e). Within this realm of differential pressure, the Young's modulus is systematically higher than the dry value for both argon and water saturation. The broad trend of decreasing modulus with increasing pressure especially beyond 60 MPa is physically implausible and probably reflects residual shortcomings in modeling the pressure dependence of the compliance of the vent tube (section 3.2.1).

5.8.2 Ultrasonic Measurements at 1 MHz

The shear and Young's moduli calculated from the ultrasonically measured wave speeds for the intact specimen YF4 both increase mildly with increasing pressure to 100 MPa (Figures 17a and 17c). The cracked specimen YF1 displays shear and Young's modulus deficits relative to the intact specimen, of ~9% at 10 MPa decreasing systematically with increasing pressure, especially for pressures <50 MPa, to only 1–2% at 100 MPa. The moduli become systematically higher when the specimen is saturated with argon (Figures 17b and 17d, reproduced as Figures 11g and 14f). Marked stiffening is noticed at differential pressures lower than 50 MPa with argon saturation, and the shear and Young's moduli gradually approach the dry moduli beyond 50 MPa. The argon saturation experiments also consist of two stages, with argon pore pressure fixed at 10 MPa and 20 MPa, respectively.

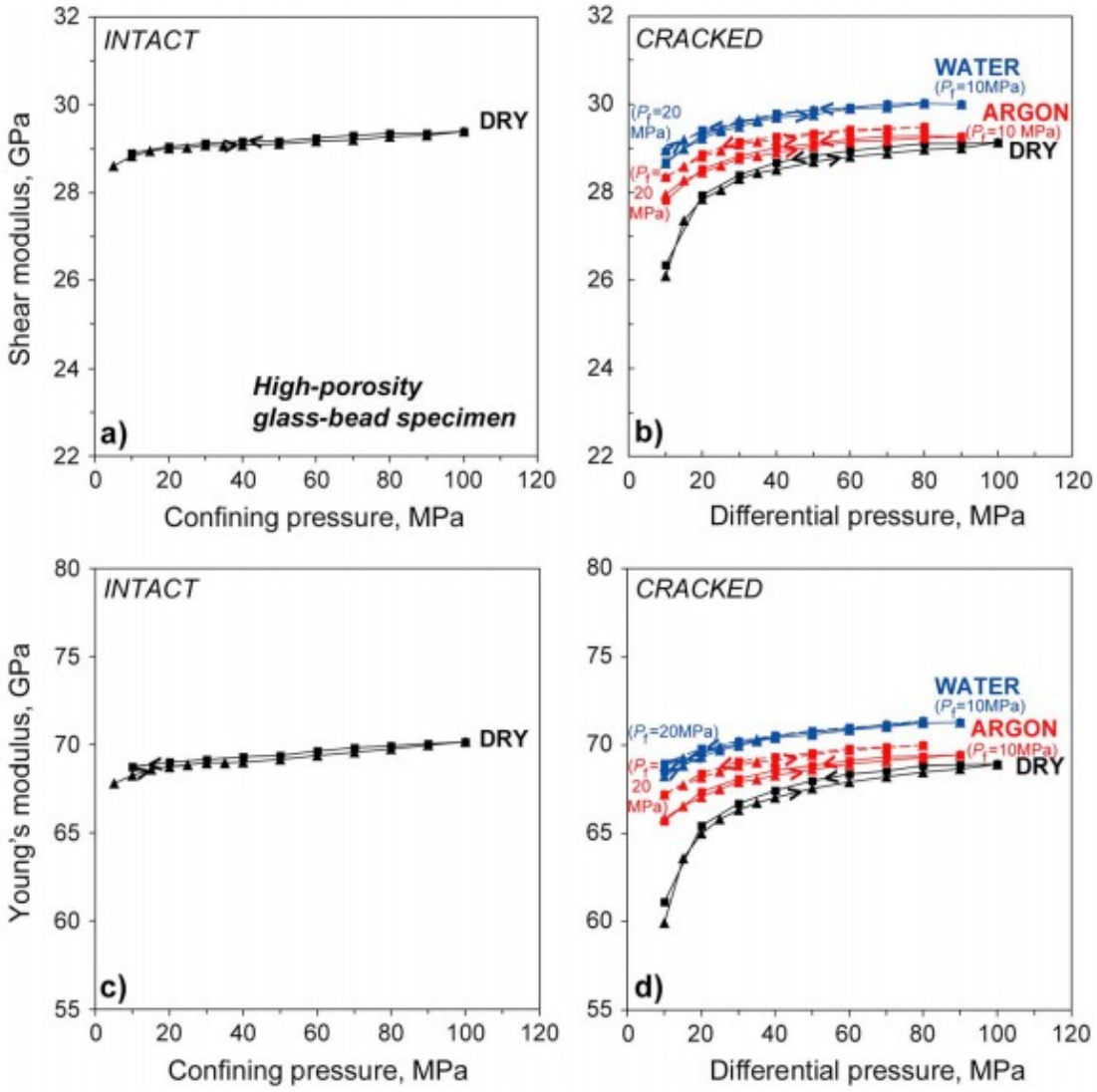

Figure 17

The dry (a) shear and (c) Young's moduli for an intact high-porosity glass bead specimen (YF4). The shear (b) and Young's moduli (d) of a cracked high-porosity glass bead specimen (YF1) under dry, argon- and water-saturated conditions. The uncertainty associated with the determined moduli is about ±1%. Arrows along curves indicate pressure path during the experiment.

At the same differential pressure, the moduli obtained with P_f = 20 MPa are higher than those for P_f = 10 MPa. With water saturation, the moduli become even higher than those measured with argon saturation. The water pressure was initially kept at 10 MPa. For the second phase of the water-saturation experiments, P_f was limited for technical reasons to 15 rather than the usual 20 MPa. Only for the lowest differential pressures (<20 MPa) were noticeably higher moduli measured with P_f = 15 MPa than those acquired with P_f = 10 MPa.

6 Discussion

6.1 Measured Strains: Heterogeneity and/or Anisotropy of Crack Distributions

There is a marked difference for pressures <10 MPa between the axial and circumferential strains for the cracked glass rod specimen (Figure 9a). The circumferential strain is closely comparable with the elastic strain expected for intact material of the appropriate bulk modulus (~40 GPa), whereas the larger axial strain is suggestive of an additional contribution from crack closure. There are two possible explanations for the purely elastic circumferential strain: either strain gauge location on the cylindrical surface between widely separated cracks (as in Figure 4, lower panel) or a minimal concentration of type B cracks at least for the glass rod material. An anisotropic distribution of crack orientations, involving dominant type B cracks, in a similarly cracked glass cylinder has been reported by Mallet et al. (2013).

6.2 Measured Permeabilities

The permeability, measured for the cracked glass rod material with water as pore fluid and the steady state flow method (Figure 8), decreases by an order of magnitude as P_d increases from 1.3 to 6.1 MPa. This variation is approximately exponential with $k = k_0 \exp(-\gamma P)$ and $\gamma \sim 0.5$. An exponential decrease of permeability in thermally cracked borosilicate glass from 7×10^{-18} to 4.5×10^{-21} m^2 with increasing differential pressure between 2 and 20 MPa was reported by Ougier-Simonin et al. (2011). Their similar results obtained with water and argon as pore fluids, yielded a well-constrained value 0.42(1) for γ. The permeability for the cracked glass specimens of the present study, as measured by the transient flow method with argon as pore fluid, decreases more mildly with increasing pressure beyond 10 MPa (Figure 8)—possibly reflecting the influence of bypass flow of argon between the cylindrical surface of the specimen and the enclosing annealed copper jacket.

Multiple data sets concerning the variation of permeability with porosity for sintered glass bead materials, ranging in bead size from 25 to 100 μm, have been recently reviewed by Bernabé et al. (2016). Amongst these data, the lowest permeabilities, measured at atmospheric pressure, range between 2×10^{-16} and 2×10^{-15} m^2 for porosities of 2–6%. That these lowest permeabilities are higher by at least 2 orders of magnitude than those measured under differential pressures >10 MPa on cracked glass bead specimens of comparable porosity in the present study suggests that cracks may also contribute to the published zero-pressure permeabilities.

Permeability was satisfactorily measured with the steady steady-flow method on a cracked glass rod specimen with water as pore fluid at differential pressures <10 MPa (Figure 8). However, attempts to use the transient flow method with water as pore fluid at differential pressures ≥10 MPa for the cracked glass media were consistently unsuccessful. Early in this study, failure to achieve pore pressure equilibration by flow of water through the cracked glass bead specimen of low porosity was attributed to the use of a

commercial workshop rust inhibitor containing oil and particulate matter with consequent potential to clog the narrow cracks. However, similar difficulties were subsequently experienced for the other cracked glass media with a rust inhibitor comprising 0.03 wt% $Na_2Cr_2O_7$ + 0.003 wt% NaOH fully soluble in aqueous solution. This result stands in marked contrast to the experience of Ougier-Simonin et al. (2011) who reported permeabilities ranging down to 5×10^{-21} m^2 for borosilicate glass with a commercial mineral water. The potential importance of chemical interaction between water and the closely spaced silicate surfaces of the cracked glass media remains for future study.

6.3 Linearity of the Subhertz Viscoelastic Behavior

In Figure 10 it was demonstrated that representative data concerning both shear modulus dispersion and associated strain energy dissipation at subhertz frequencies are adequately fitted by an Andrade creep function model. Such simultaneous description of the dispersion and dissipation provides evidence of consistency with the Kramers-Kronig relations of linear viscoelasticity (e.g., Nowick & Berry, 1972). This observation, along with insensitivity of modulus and dissipation to variation of peak strain amplitude ($<10^{-5}$) suggests that the strain amplitudes realized in forced oscillation and the even lower strains of the resonant bar and ultrasonic techniques of this study, consistently probe the linear regime.

6.4 Pressure-Induced Crack Closure: Generalities

Substitution into equation 3 of the Young's modulus (~70 GPa) typical of soda-lime-silica glass and a nominal crack aspect ratio of 10^{-3} (e.g., Table 3), yields an estimated crack closure pressure of 70 MPa. The measured moduli and permeability vary strongly with differential pressure P_d for low values of P_d but become progressively much more mildly pressure dependent at higher pressures. The pressure dependence of permeability is relatively mild for differential pressures >20 MPa, especially for the glass bead specimens (Figure 8). Most of the pressure dependence of the elastic moduli is similarly observed at confining/differential pressures <30 MPa (summary in Figures 11 and 14). Such pressure dependencies are thus plausibly attributed to the pressure-induced closure of cracks—with aspect ratios mainly $<4 \times 10^{-4}$, significantly smaller than those estimated from the light micrographs (Table 3). The observation that the moduli measured for the cracked glass bead materials consistently closely approach (within 1 and 2% for G and E, respectively) those for the corresponding uncracked material at the highest pressures P_{max} attests to essentially complete crack closure.

In contrast, for the cracked glass rod specimens, it was previously noted that substantial modulus deficits (8 and 10% for G and E, respectively) remain at the highest pressure P_{max}(100 MPa) of the ultrasonic measurements (Figure 15). Similarly low maximum values of shear modulus near 28 GPa were observed for the cracked glass rod specimen tested in torsional forced oscillation (Figure 11). For the resonant bar measurements on a cracked glass rod specimen of larger diameter (38 rather than 15 mm), somewhat

smaller deficits of 4% and 6% in G and E, respectively, were measured at the highest confining/differential pressure of 24 MPa. Only in ultrasonic measurements on cracked glass rod specimen FDS1 prior to the development of a throughgoing fracture were modulus deficits <2% at P_{max} observed. These observations suggest that pressure-induced closure of the thermally generated cracks is somewhat variable but must generally be inhibited to a greater degree than in the glass bead specimens. In the absence of pores within the dense glass rod, the creation of thermal cracks may be a more energetic process resulting in some comminution of material evident in the generally more irregular crack edges (Figure 6b). The strong pressure sensitivity of elastic moduli at differential pressures <30 MPa might reflect the closure of cracks free of fragmented material. It is suggested that a substantial proportion of the total crack porosity remains propped open by fragmented material at P_{max}—explaining the substantial residual modulus deficits generally observed for the glass rod material.

6.5 Aspect Ratio Distribution Functions for Crack Density and Crack Porosity

A more detailed analysis involves inversion of the pressure-dependent elastic moduli inferred from the dry ultrasonic P and S wave velocities for the pore and crack microstructure of each synthetic sample. In the first step, the bulk and shear moduli derived from the measured P and S wave velocities at the highest pressure, P_{max} (~100 MPa), reached in the laboratory experiment are compared with those for the fully dense soda-lime-silica glass. The inferred modulus deficits along with the measured equant porosity ϕ_{op} (Table 2) allow estimation of the mean aspect ratio of the pores that remain open at P_{max} (section 4.1). The mean aspect ratios of the nonclosable pores thus inferred are 0.35 and 0.45 for the glass bead specimens, of low and high porosity, respectively. The aspect ratios of these nonclosable pores are, reasonably, substantially less than 1 as for a perfect spherical pore but much higher than those of order of 10^{-3} for the closable thin cracks. The glass medium including such nonclosable pores forms the matrix within which closable cracks are embedded.

The bulk and shear moduli derived from the pressure-dependent ultrasonic wave speeds measured under dry conditions are then analyzed with equations A5 and A6 of Appendix Appendix A to obtain the effective crack density $\Gamma(P)$ which is fitted to a smooth interpolating function (Figures 18a, 18d, and 18g). For such relatively low crack densities (<0.1 for P_d > 10 MPa), closely similar results would be expected from simpler models in which crack interactions are ignored (e.g., Benson et al., 2006; Kachanov, 1993).

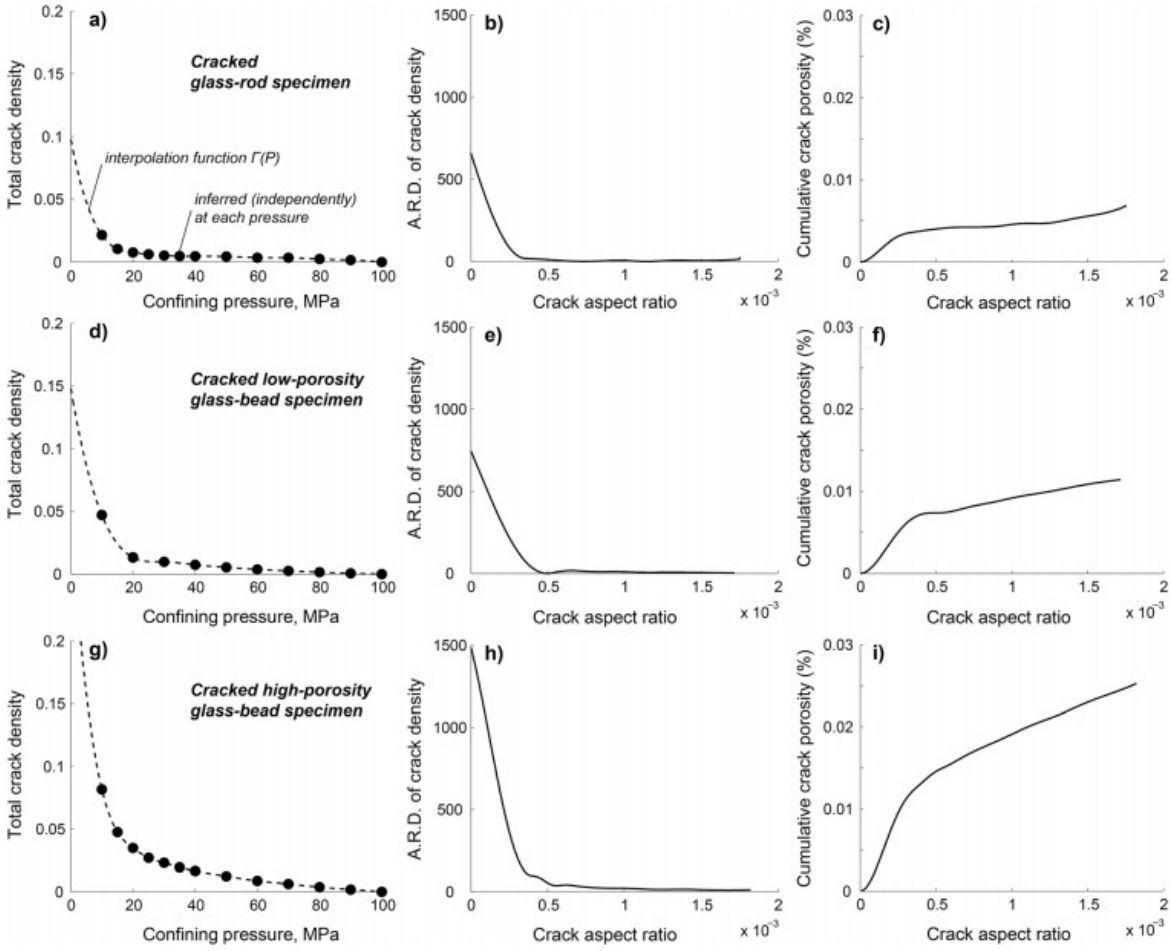

Figure 18

(a, d, and g) Effective crack density, Γ, as function of pressure, (b, e, and h) zero-pressure aspect ratio distributions $\gamma(\alpha)$ for crack density (equation A9), and (c, f, and i) associated cumulative crack porosities $C(\alpha)$ (equation A11) on the glass rod, low-porosity glass bead, and high-porosity glass bead specimens, inferred from the measured pressure-dependent ultrasonic P and S wave velocities.

The aspect ratio distribution $\gamma(\alpha)$ for crack density (equation A9) and cumulative crack porosity $C(\alpha)$ (equation A11) are finally inferred from the pressure dependent crack density $\Gamma(P)$ for each cracked sample. The aspect ratio distribution $\gamma(\alpha)$ for crack density for each specimen (Figures 18b, 18e, and 18h) decreases monotonically and strongly with increasing aspect ratio $\alpha < 4 \times 10^{-4}$, in accord with the previous inference from a single representative closure pressure. However, cracks of higher aspect ratio (to $\sim 1.8 \times 10^{-3}$) also contribute significantly to the cumulative crack porosity $C(\alpha)$ (Figures 18c, 18f, and 18i). The inferred aspect ratios are mainly significantly lower than the observed average aspect ratios of $\sim 2 \times 10^{-3}$ and $\sim 1 \times 10^{-3}$(Table 3), for the glass rod and glass bead specimens, respectively. The discrepancy may be explained in part by overestimation of crack apertures from polished sections.

The total closable crack porosity of each sample is indicated by the cumulative porosity $C(\alpha)$ at the highest aspect ratio for closable cracks (Figures 18b, 18d, and 18f). The marked increase in $C(\alpha)$ near $\alpha = 2 \times 10^{-4}$ corresponds to a prominent maximum for the aspect ratio distribution $c(\alpha)$ for crack porosity (equation A10) not plotted in Figure 18 (see, e.g., David & Zimmerman, 2012). The closable crack porosities thus estimated for the glass rod, low-porosity, and high-porosity glass bead specimens are 0.006%, 0.012%, and 0.025%, respectively. These values are lower by factors of 6–60 than those determined by the volume increases on thermal cracking, which are 0.35%, 0.08%, and 0.14% for the ultrasonically measured glass rod, low-porosity glass bead, and high-porosity glass bead specimens, respectively (Table 2). X-ray absorption data reported in Figure 7 indicate an average closable porosity of ~0.14% for glass rod specimen FDL2—an only modest fraction of the total crack porosity (0.74%) determined by mensuration on the same specimen (Table 2), but much larger than that inferred in Figure 18c.

The discrepancies between the crack porosities directly determined by mensuration and the closable crack porosities inferred from the measured moduli are too large to be explained by a nonclosable fraction of the crack porosity. Instead, it is suggested that much of the observed crack porosity in our glass materials, thermally cracked at ambient pressure, might be associated with a spatially uniform parting between the opposite sides of a crack, which is effectively of zero aspect ratio. Such porosity would be closed by negligibly low pressures—below the 10 MPa threshold for the ultrasonic wave speed measurements—and therefore potentially be inadequately represented by extrapolation of the interpolating function fitted to $\Gamma(P)$ values for $P > 10$ MPa. The aspect ratio distributions for both crack density $\gamma(\alpha)$ and crack porosity $c(\alpha)$ might accordingly be seriously underestimated for low aspect ratios ($<2 \times 10^{-4}$).

6.6 The Effect of Fluid Saturation on the Measured Elastic Moduli

6.6.1 Broad Trends

Changes of the elastic moduli associated with fluid saturation for each of the three glass materials over the entire frequency range of this broadband study are summarized in Figure 19. Here the variation in modulus due to fluid saturation is expressed as a percentage change with respect to the dry modulus measured at the same pressure and frequency with the same technique on the same sample. An obvious advantage of using percentage change in modulus is that any systematic differences between dry moduli measured by different techniques, including the effects of any hysteresis associated with pressure cycling, are excluded.

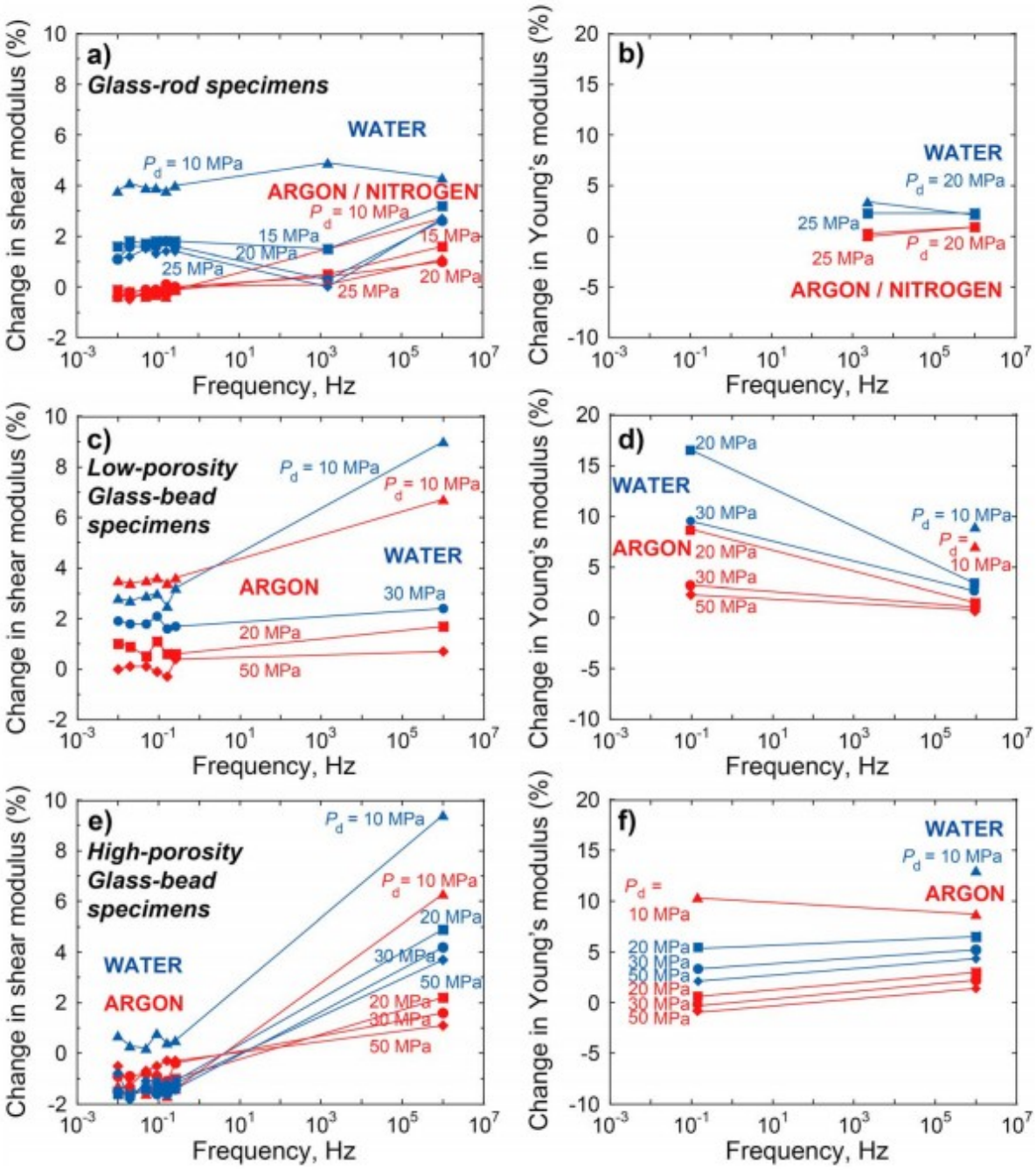

Figure 19

Percentage changes in shear modulus and Young's modulus (a and b) for the glass rod specimens, (c and d) for the low-porosity glass bead specimens, and (e and f) for the high-porosity glass bead specimens, with either argon (red) or water (blue) saturation at differential pressures <50 MPa and subhertz to megahertz frequencies. Values >20% plot off-scale in (d) and (f). The very large values for P_d = 10–20 MPa are probably partly attributable to substantially reduced interfacial compliance.

Saturation, whether with gaseous (argon or nitrogen) or condensed (water) fluids, results in generally higher values of both shear and Young's moduli, respectively, *G* and *E*, for each of the three types of sample at the

intermediate to ultrasonic frequencies of this study (Figure 19). The observation of systematically higher shear moduli for fluid (especially water) saturation is consistent with the presence of an incompressible pore fluid, within which pressure gradients are unrelaxed by fluid flow, that is, conditions within the *saturated isolated* regime. In marked contrast, a shear modulus equal to that of the dry medium is expected for *saturated isobaric*conditions.

Drainage of the specimen to an external reservoir is required if the bulk modulus is also to be unaffected by fluid saturation. Such conditions are expected at sufficiently low frequencies. At the subhertz frequencies of this study, the shear modulus for the high-porosity glass bead specimen is certainly not increased by fluid saturation (with either argon or water saturation) but may in fact decrease significantly (Figures 11 and 19). The low-frequency Young's modulus data for this specimen (Figures 14 and 19) suggest increased E (and therefore K) on water saturation for $P_d \leq 20$ MPa—qualitatively consistent with expectations for the saturated isobaric regime rather than drained conditions.

Intermediate behavior, apparently transitional between saturated isolated and isobaric regimes, is observed in the low-frequency shear mode data for the glass rod specimen, where the shear modulus is significantly increased by water saturation for $P_d \leq 30$ MPa, but not by argon saturation. The data for the low-porosity glass bead specimen are somewhat more equivocal but both shear and Young's moduli are apparently increased by fluid saturation (both argon and water) for $P_d \leq 30$ MPa (Figures 11, 14, and 19).

6.6.2 Effects of Fluid Density, Trace Amounts of Moisture Under Nominally Dry Conditions, and Further Cracking During Pore Pressure Cycling

Increased P wave speeds resulting from water saturation of sandstones have been commonly reported at kilohertz-megahertz frequencies (Gregory, 1976; King, 1966; Winkler, 1985; Winkler & Nur, 1982). However, for S wave speeds, both increases (Baechle et al., 2005; David et al., 2013; King, 1966) and decreases (Nur et al., 1980; Winkler, 1985; Winkler & Nur, 1982) on fluid saturation have been reported.

Increased S wave speeds observed at sufficiently high frequencies are normally attributed to conditions that are unrelaxed with respect to local or squirt flow of relatively incompressible fluid. Such fluid-related increase of the shear modulus becomes less significant as cracks are progressively closed by pressure. Because elastic wave speeds vary as the square root of the appropriate elastic modulus divided by the density, fluid-related changes in modulus and density compete with each other. The increased modulus dominates for high crack densities at low differential pressure, whereas increased density can dominate at high values of P_d, especially for rocks of high nonclosable porosity. The interplay between these two effects can result in a situation where shear wave speeds are higher water-saturated than dry for low P_d, but the converse situation applies at high P_d (David et al., 2013;

King, 1966). In this study, however, the “fluid-saturated” wave speeds are invariably higher than the corresponding dry wave speeds—presumably because the influence on moduli of the pressure-dependent crack density dominates over the density changes for materials of relatively low total porosity.

The adsorption of water molecules especially on silicate mineral surfaces, is capable of significantly reducing the surface free energy at asperities across which adjacent “grains” make contact, resulting in lower effective elastic moduli and increased dissipation (Adam et al., 2006; Adelinet et al., 2010; Pandit & King, 1979; Pimienta et al., 2014; Spencer, 1981; Tittmann, 1978; Tutuncu & Sharma, 1992).

Saturation of the pore space with argon at relatively high pressure should tend to remove any trace amounts of adsorbed/bulk water from such grain contacts. Flushing of adsorbed water from the pore space might therefore result in a tendency toward increased moduli measured either under argon-saturated relative to dry conditions, or in dry measurements repeated following argon saturation. The slightly higher shear moduli measured on cracked glass rod specimen FDSL1 (Figure 11) in the repeated dry measurements might be explained in this way.

For the thermally cracked specimen of the high-porosity glass bead material tested in low-frequency forced oscillation, the absence of a systematic increase of the shear modulus with fluid saturation has been attributed to conditions within the saturated isobaric regime. In fact, the shear modulus actually *decreases* upon fluid saturation (Figures 11, 14, and 19)—suggesting that the crack density might inadvertently have been increased during cycling of the pore pressure.

6.6.3 Characteristic Frequencies for Draining and Squirt Flow

It has long been predicted that mechanical testing at progressively increasing frequency will probe a succession of fluid flow regimes, separated by characteristic frequencies (Figure 1). As explained in section 4.2.2, the draining frequency f_{dr} relevant to gas saturation of equant porosity is prescribed by equation 4a, which bears a close similarity with that for the rate constant A for pore pressure equilibration (equation 2), each parameter being proportional to kK_f/η. The alternative equation 4b clearly applies to water saturation of thermal cracks of aspect ratio 2×10^{-4} in a glass medium ($G \sim 31$ GPa and $\nu \sim 0.21$), where f_{dr} is lower than $kK_f/\phi\eta l^2$ by a multiplicative factor of 180.

Draining frequencies estimated from equations 4a and 4b for representative experimental conditions are presented in Table 4. The frequencies for the draining of pore fluid from the stressed cracked glass specimens are consistently very low—ranging from ~0.05 to ~8 mHz (Table 4). It is inferred that undrained conditions are generally expected even at the 0.01–1 Hz frequencies of the forced oscillation tests. Use of the

approximation $C_{pp} \approx C_{pc}$ in equation A14is obviously most clearly appropriate for the cracked glass rod material, and accordingly, the estimated draining frequencies for this material are considered to be more robust than those for the glass bead specimens containing both cracks and pores.

Table 4

Characteristic Frequencies f_{dr} and f_{sq} for Draining and Squirt Flow, Respectively, Under Representative Conditions of Confining and Pore Pressure for Each of the Three Types of Cracked Glass Medium Estimated Through Equations (4a), (4b), and (5)

Saturant	P_d (MPa)	P_f (MPa)	ϕ_{conn}	k (10^{-19} m^2)	K_f (GPa)	η (mPa/s)	f_{dr} (mHz)	f_{sq} (kHz)
				Glass rod				
Ar	53	39	0.003	0.9	0.055	0.043	1.2	1.3
Ar	11	87	0.003	7.4	0.21	0.065	7.9	0.8
H_2O	10	10	0.003	7	2.2	1.0	0.5	0.05
				Low-ϕ glass bead				
Ar	91	9	0.01	1.0	0.009	0.029	0.3	1.9
Ar	12	87	0.01	8.1	0.21	0.066	2.5	0.8
H_2O	10	10	0.01	7	2.2	1.0	0.2	0.05
				High-ϕ glass bead				
Ar	74	17	0.03	2.5	0.017	0.033	0.3	1.7
Ar	17	82	0.03	6.4	0.19	0.063	0.7	0.9
H_2O	10	10	0.03	7	2.2	1.0	0.05	0.05

Note. For saturation of each of the media with highly compressible argon, (P_c, P_f) conditions have been chosen to span most of the range of pore pressure P_f accessed during the paired permeability and forced oscillation tests. For saturation with water, a relatively incompressible pore fluid, the estimates apply to the representative conditions (P_c, P_f) = (20, 10) MPa and an (argon) permeability $k = 7 \times 10^{-19}$ m^2, typical of $P_d \sim 10$ MPa (Figure 8). Values for the other variables were fixed as follows: $l = 75$ mm (half length of the specimen), bulk modulus $K_0 = 43$ GPa, shear modulus $G = 31$ GPa, and $\nu = 0.21$ from ultrasonic measurements at $P_c = 20$ MPa for the uncracked glass rod specimen (Li, 2016); $\alpha = 2 \times 10^{-4}$ as a representative aspect ratio for the thermal cracks (Figure 18).

Because the shear modulus for the saturated isobaric regime is that of the dry cracked medium, the shear modulus is expected to be unaffected by draining. As Young's modulus combines the bulk and shear moduli (equation 6), measured Young's moduli will reflect the expected sensitivity of bulk modulus to water saturation in the undrained regime. That no such relaxation is observed in the flexural oscillation tests on the glass bead materials is consistent with the f_{dr} estimates of Table 4.

The characteristic frequency f_{sq} for local squirt flow between thin cracks, that separates the saturated isolated and saturated isobaric regimes has been estimated from equation 5 for representative conditions, with an indicative crack aspect ratio of 2×10^{-4}, are presented in Table 4. As $f_{sq} \sim \alpha^3$, the estimated frequency is potentially sensitive to any variation of the assumed crack aspect ratios, for example, with changing pressure, but modeling suggests that this effect is minor. For argon saturation, the squirt frequencies are ~1 kHz—comparable with the frequencies of the resonant bar tests but significantly lower than the MHz frequency of the ultrasonic measurements. Accordingly, the ultrasonic measurements are clearly expected to probe the saturated isolated regime, whereas the resonant bar tests on the cracked glass rod specimen are conducted under conditions

close to the boundary between the saturated isolated and saturated isobaric regimes. For water saturation, a much lower squirt frequency near 40 Hz is calculated—comfortably consistent with saturated isolated conditions for the resonant bar tests.

6.6.4 Fluid Flow Regimes

The observed changes in elastic moduli on fluid saturation, and the characteristic frequencies estimated for stress-induced fluid flow, are sources of complementary information concerning the attribution of experimental data to the various fluid flow regimes. Saturated isolated conditions are clearly expected for ultrasonic measurements at ~1 MHz from the characteristic frequencies estimated for squirt flow, and this expectation is reinforced by the observed substantial stiffening in shear, especially for water saturation, for each of the three types of material. However, attribution of the resonant bar and forced oscillation data to fluid flow regimes is less straightforward.

For the glass rod specimen, water saturation results in substantial increases in shear modulus at both kilohertz and subhertz frequencies (Figures 11 and 19). Indeed, the increase of Young's modulus on water saturation at kilohertz frequencies (Figure 14) is so large as to suggest a possible contribution from elimination of residual interfacial compliance. The fact that water saturation results in a consistent ~4% increase in shear modulus at P_d = 10 MPa across the entire frequency band from 10 mHz to 1 MHz (Figure 19) suggests that all such data belong to the saturated-isolated regime. However, the implication of a squirt frequency f_{sq} < 10 mHz is a remarkably low crack aspect ratio ($\leq 10^{-5}$) controlling squirt flow. The contrasting results obtained at subhertz frequencies for argon saturation suggest saturated-isobaric conditions. The small increase in shear modulus on nitrogen saturation (with P_f only 3.1 MPa) in the resonant bar measurements at kilohertz frequencies, marginally greater than the f_{sq} estimated for argon saturation (Table 4), may signify the transition from saturated isobaric to saturated isolated conditions with increasing frequency beyond ~1 kHz.

For the low-porosity glass bead specimen, argon saturation results in a substantial increase (3.6%) in shear modulus at subhertz frequencies only for (P_d, $P_{f)}$ ~ (10, 89) MPa. Comparable stiffening is observed for water saturation with (P_d, $P_{f)}$ ~ (11, 15) MPa; a systematically higher shear modulus is observed with increasing P_d in the range 16–31 MPa (Figure 11). At the megahertz frequency of ultrasonic measurement, the increases in shear modulus for argon and water saturation are 6.7% and 9.0% (Figure 19). The smaller modulus differences associated with fluid saturation at subhertz frequencies suggest conditions transitional between the saturated-isolated and saturated-isobaric regimes, apparently requiring a substantially lower squirt frequency and hence crack aspect ratio than estimated in Table 4, as for the glass rod specimen.

For the high-porosity glass bead specimen, a shear modulus insensitive to fluid saturation has been observed at subhertz frequencies, indicating either drained or saturated-isobaric conditions (Figures 11 and 19). Further evidence is provided by the measured Young's modulus, which seems to increase with both argon and water saturation at the lowest differential pressures (Figures 14 and 19)—suggesting undrained, that is, saturated isobaric, conditions. The inferences concerning the fluid flow regimes relevant for the various specimens and measurement techniques are summarized in Table 5.

Table 5
Fluid Flow Regimes Probed by Modulus Measurements at Subhertz, Kilohertz, and Megahertz Frequencies on the Cracked Glass Media

		Inferred fluid flow regime		
Specimen type	Saturant	10–260 mHz	1–3 kHz	1 MHz
Glass rod specimen	Water	Saturated isolated	Saturated isolated	Saturated isolated
	Argon or nitrogen	Saturated isobaric	Transitional	Saturated isolated
Low-porosity glass bead specimen	Water	Transitional	—	Saturated isolated
	Argon	Transitional	—	Saturated isolated
High-porosity glass bead specimen	Water	Saturated isobaric	—	Saturated isolated
	Argon	Saturated isobaric	—	Saturated isolated

6.6.5 The Saturated-Isolated Regime

All specimens tested at megahertz frequencies belong to the saturated isolated regime. Such an attribution is clearly justified by the observed stiffening of shear modulus for all specimens under argon- or water-saturated conditions (Figures 11 and 19), which would not be predicted by the low-frequency Biot-Gassmann model. In addition, the Biot-Gassmann estimates for Young's modulus, which are calculated from dry ultrasonic data using known values of specimen porosity (e.g., Le Ravalec & Guéguen, 1996), lie well below experimental measurements of Young's modulus under both argon and water-saturated conditions, as illustrated in Figure 20 for the high-porosity glass bead specimen. The Biot-Gassmann model predicts essentially no stiffening of Young's modulus under argon saturation (at least at pore pressure of 10 MPa), due to the high compressibility of the fluid. Under water saturation, the Biot-Gassmann model accounts for only about 25% of the observed stiffening. On the glass rod and low-porosity glass bead specimen, the Biot-Gassmann model equally underestimates both shear and Young's moduli (or P and S wave velocities) at ultrasonic frequencies (cf. David & Zimmerman, 2012; Pimienta et al., 2015a).

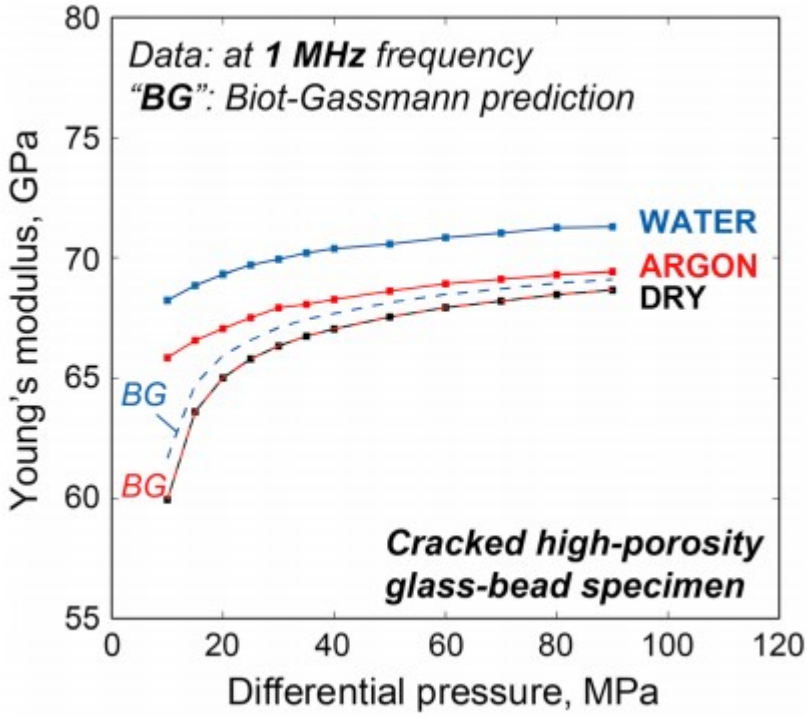

Figure 20

Young's modulus inferred from ultrasonically measured *P* and *S* wave speeds for the cracked high-porosity glass bead specimen saturated with either argon or water (in each case at a pore pressure of 10 MPa), compared with low-frequency Biot-Gassmann predictions based on the dry modulus.

Within the saturated-isolated regime, stress-induced pore pressure differentials even between adjacent parts of the crack-pore network remain unrelaxed by fluid flow, so that the effective elastic moduli for the saturated isolated regime can be appropriately modeled by differential effective medium theory. The microstructure of the crack-pore network, involving the aspect ratios of both nonclosable pores and of closable thin cracks, has been inferred by inversion of the pressure-dependent dry moduli determined from the ultrasonic wave speeds (section 6.5) with the methods of sections 4.1 and 4.2. The effective elastic moduli for the three synthetic glass media, saturated with either argon or water, are then predicted from such inferred microstructure and fluid properties through differential effective medium theory (section 4.2.2).

The differential effective medium model predicts close convergence with increasing differential pressure amongst the modulus-differential pressure trends for dry and fluid-saturated conditions (Figure 21). Such convergence is the result of the closure by P_{max} of all of the modeled crack porosity, and the limited impact upon the moduli of fluid saturation of the remaining more nearly equant, and connected, nonclosable porosity. The ultrasonically measured wave speed-differential pressure trends converge closely (within ~0.5%) especially for the glass bead materials (Li, 2016), but the associated

modulus-differential pressure trends are offset by as much as 2.0(±2)% for the high-porosity glass bead material (Figure 21) mainly reflecting the effect of fluid saturation of the connected porosity on density. The model seems to describe the effect of fluid saturation better for the bulk modulus than for the shear modulus (Figure 21), allowing closer prediction of *P* wave velocity than *S* wave velocity (Li, 2016).

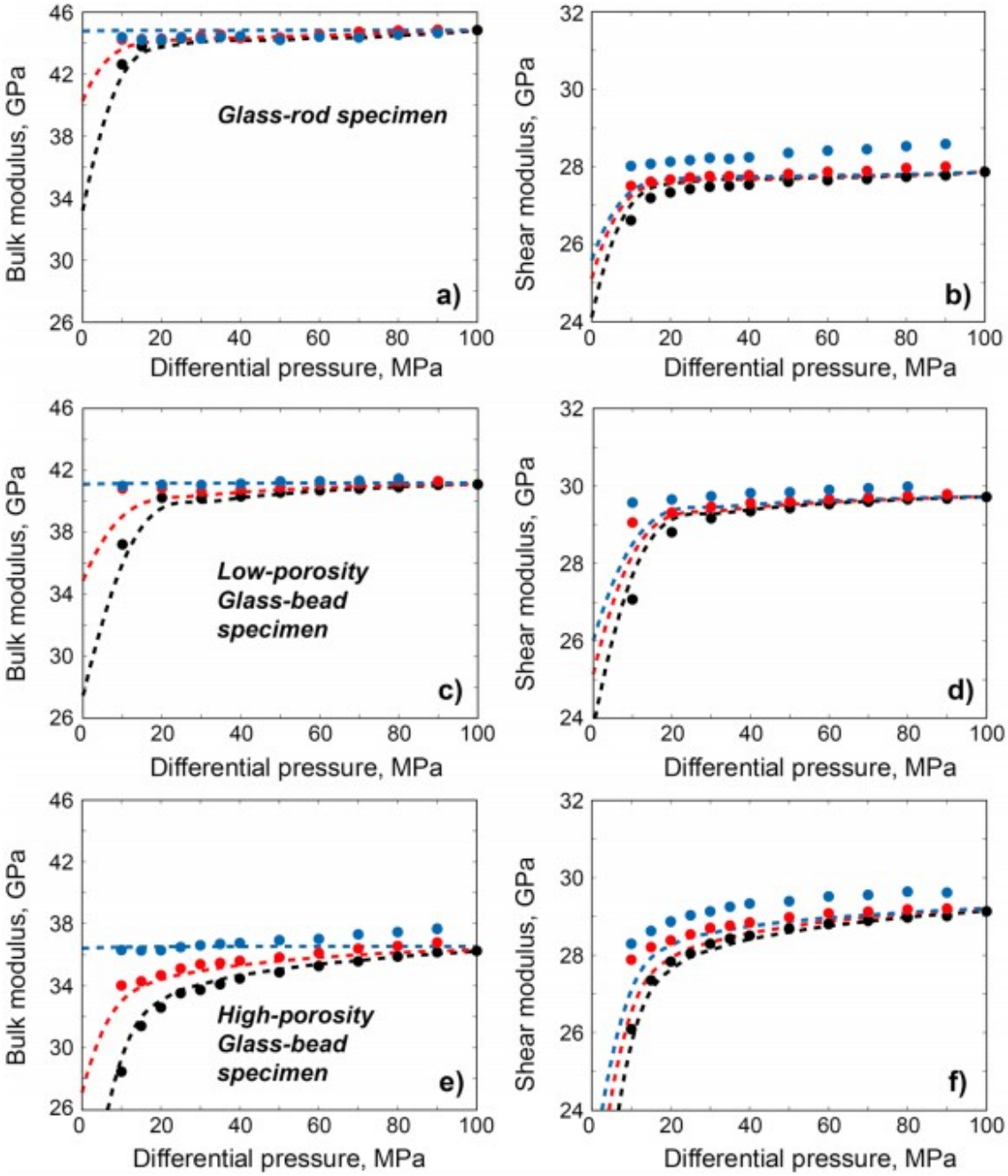

Figure 21

Bulk and shear moduli (dashed curves) predicted for fluid saturation of the dry cracked media through the differential effective medium model (David & Zimmerman, 2012) compared with those (symbols) inferred from the megahertz wave speed measurements. (a and b) Glass rod material, (c and d) low-porosity glass bead specimen, and (e and f) high-porosity glass bead medium. Dry, argon- and water-saturated conditions are indicated by the black, red, and blue colors, respectively. For the cracked glass bead specimens, under conditions of argon- and water-saturation, model predictions are based on the assumption that only the connected fraction ϕ_{He} of total equant porosity ϕ_{op} is saturated, while the remaining fraction ($\phi_{op} - \phi_{He}$) is taken as dry (Table 1).

The competition between the effects of fluid saturation on modulus and density is reflected in a predicted crossover of velocity-pressure trends for dry and water-saturated conditions, which is not observed in the experimental data (Li, 2016). Concerning modeling of the behavior of the glass rod specimen FDS3, it should be recalled that substantial residual modulus deficits at P_{max} suggest closure of only a fraction of its 0.35% crack porosity. However, no attempt has been made to include the influence of the unknown amount of nonclosable porosity in this material in the effective medium calculation.

The failure to achieve a broadly satisfactory reconciliation between the predictions of the effective medium model and the observations raises the following issues:

1. Both water permeability (Figure 8) and strain gauge (Figure 9) measurements indicate a significant amount of crack closure occurring below 10 MPa. However, the lack of ultrasonic velocity data below 10 MPa means that the crack density function $\Gamma(P)$ is unconstrained at lower pressure and therefore necessarily extrapolated from higher pressures.
2. The model was initially developed for sandstones (David & Zimmerman, 2012) that often possess an unusually narrow distribution of crack aspect ratios and may be less suitable for thermally cracked synthetic glass materials: in particular, the idealized thin spheroidal shape of the model cracks may be less appropriate for the uniform partings of the thermal cracks in these glass media.
3. The use of an elastically isotropic model may be questionable for thermally cracked materials with their potentially significant heterogeneity and preferred crack orientations. The neglect of heterogeneity and anisotropy may compromise the estimates of crack porosity. However, the distributions of crack aspect ratios inferred from the pressure sensitivity of the elastic moduli and the qualitative influence of fluid saturation on the elastic moduli of any given cracked specimen should be more robust.
4. Higher than predicted moduli and wave speeds for fluid saturation at the highest pressures might reflect the influence of residual unclosed cracks inadequately accounted for by the inferred average aspect ratio for the nonclosable porosity in each of the glass bead specimens.

6.6.6 The Magnitude of Fluid-Related Dispersion

The influence of fluid saturation at each frequency is appropriately expressed as a percentage change in modulus, so that the percentage dispersions in shear modulus D_G and Young's modulus D_E are defined as

$$D_G = \Delta G_{HF} - \Delta G_{LF}, \quad (9)$$

$$D_E = \Delta E_{HF} - \Delta E_{LF} \quad (10)$$

where ΔG_{HF} and ΔE_{HF} are the percentage changes in shear and Young's modulus at megahertz, respectively, and ΔG_{LF} and ΔE_{LF} are the percentage changes in shear and Young's modulus at subhertz frequencies, respectively.

The changes in moduli due to fluid saturation across the broad frequency band encompassed by this study have been presented in Figure 19. We have found no evidence in this study of drained conditions—a circumstance attributable to the combination of very low permeabilities and high crack compliances of the cracked synthetic glass materials. Thus, significant dispersion is associated only with the transition with increasing frequency between the saturated isobaric and saturated isolated regimes, and fluids will generally have their greatest influence when crack densities are largest at low differential pressures.

For the glass rod specimen, we previously inferred that saturated-isolated conditions apparently prevail at all frequencies for water saturation so that there is no discernible dispersion, whereas argon saturation probes saturated isobaric, transitional, and saturated isolated conditions at subhertz, kilohertz, and megahertz frequencies, respectively, resulting in ~3% dispersion of shear modulus across the entire frequency range (Figure 19a).

For the argon-saturated low-porosity glass bead specimen, a dispersion of ~3% is observed for shear modulus at a differential pressure of 10 MPa between subhertz and megahertz frequencies. Water saturation doubles the dispersion, giving ~6%, between subhertz and megahertz frequencies (Figure 19c). These reflect the transition, for both argon and water saturations, to saturated isolated conditions. The dispersions in shear modulus are ~8% and ~9% for argon and water saturation, respectively, between subhertz and megahertz frequencies on the high-porosity glass bead specimen at the differential pressure of 10 MPa (Figure 19e), reflecting the transition from saturated isobaric to saturated isolated conditions.

The dispersion, strongest at the lowest commonly accessed differential pressure of 10 MPa, progressively decreases with increasing differential pressure for each type of sample with either argon or water saturation—reflecting the previously discussed diminishing crack porosity. As a result, the shear dispersion D_G is a function of pressure. Winkler (1985, 1986) noticed a similar trend of reduced dispersion of *P* and *S* wave velocities by elevated pressure on Berea sandstones with brine and oil saturation. Similar pressure dependencies of the extent of bulk modulus dispersion between seismic and ultrasonic frequencies have been reported for Icelandic basalt

(Adelinet et al., 2010; Fortin et al., 2014) and for Fontainebleau sandstones (Fortin et al., 2014; Pimienta et al., 2015a, 2015b). Dispersion of elastic moduli and/or frequency-dependent attenuation have also been observed in other forced oscillation studies of various rock types: sandstones (Mikhaltsevitch et al., 2014), carbonates (Adam & Batzle, 2008; Adam et al., 2006, 2009; Batzle et al., 2006), shales (Delle Piane et al., 2014), and quartzites (Schijns et al., 2018).

7 Conclusions and Future Directions

In this paper, we have reported the results of an extensive experimental broadband study of the seismic properties of synthetic soda-lime-silica glass media. Cylindrical specimens, prepared either from dense glass rod or aggregates of sintered glass beads of 2%–5% residual porosity, were subjected to thermal cracking by quenching from high temperature into water. Mensuration and mechanical tests, conducted before and after thermal cracking, provide direct information concerning both the magnitude of the introduced crack porosity and its influence on the effective elastic moduli. The network of narrow thermal cracks results in systematically very low permeabilities, $<10^{-18}$ m^2 for $P_d \geq 10$ MPa, 2–3 orders of magnitude below those typical of relatively tight sandstones. Analysis of the pressure dependence of the modulus deficits attributable to open cracks in the dry medium yields a pressure-dependent effective crack density from which the distribution of crack aspect ratios and cumulative closable crack porosity are inferred. The closable porosity estimated in this way is substantially less than that inferred by in situ CT scanning of a glass rod specimen and systematically much less than the total crack porosity directly measured at atmospheric pressure, suggesting that the thermal cracks may constitute a distinctive microstructure—with uniform partings of near-zero effective aspect ratio that contribute much of the crack porosity—but are closed at lower pressures than the usual threshold (10 MPa) for forced oscillation and ultrasonic methods.

Concerning the influence of fluid saturation on the seismic properties, the low permeabilities for these cracked media result in unusually low draining frequencies, estimated to be of order 0.01–1 mHz, providing access to undrained conditions across the entire 10 mHz–1 MHz frequency range of this study. At the MHz frequency of ultrasonic wave propagation, increased moduli for each of the cracked media with fluid saturation are diagnostic of saturated-isolated conditions. However, the influence of fluid saturation (especially with water) on the shear moduli measured at MHz frequencies is stronger than is readily reconciled with differential effective medium modeling of the saturation of both closable cracks and of the connected nonclosable porosity.

Water saturation of the cracked glass rod specimen results in substantial increases (~4%) of the shear modulus also at kilohertz and subhertz frequencies. Evidence of saturated-isolated conditions at such low

frequencies requires squirt frequencies <10 mHz and thus very low effective aspect ratios $<10^{-5}$ for squirt between cracks of different orientation. The increased shear moduli measured at subhertz frequencies in forced oscillation for the water-saturated low-porosity glass bead specimen require a similar interpretation. In marked contrast, the shear modulus measured in forced oscillation on the high-porosity glass bead specimen is insensitive to fluid saturation as expected of the saturated isobaric regime.

This broadband study of seismic properties under undrained conditions reveals behavior that is generally dispersive and inferred to result from stress-induced squirt flow. For example, for the cracked and fluid-saturated glass bead materials of high-porosity, forced oscillation measurements at subhertz frequencies yield the dry shear modulus in accord with Gassmann's prediction, whereas higher shear moduli at megahertz frequencies are attributed to the saturated-isolated regime. For the glass rod and low-porosity glass bead materials, however, crack aspect ratios are evidently sufficiently low as to yield squirt frequencies for water <10 mHz allowing saturated-isolated conditions to persist to subhertz frequencies resulting in no measurable dispersion between 10 mHz and 1 MHz. Such experimental observations of dispersion resulting from stress-induced fluid flow reinforce theoretical predictions (Guéguen & Sarout, 2011) and thus confirm the need for care in the seismological application of laboratory ultrasonic data.

Promising directions for future work include the following:

1. Replacement of the vertical tubular mould for sintering of glass beads with a larger rectangular box allowing horizontal coring of specimens potentially more uniform in porosity;
2. Further investigation of crack microstructures including the crack roughness reflecting apparently more energetic cracking of the glass rod material, the possible influence of glass bead size on the radial heterogeneity of crack distribution, variation of the peak temperature from which the specimens are quenched potentially allowing variation of crack aspect ratios and/or crack density, and the possible stabilization of crack microstructures through annealing at high temperature following cracking;
3. Application of automated methods for crack characterization from SEM images (Arena et al., 2014);
4. Further refinement of the methods used for estimation of Young's modulus from the measured flexural compliance;
5. Use of multipath ultrasonic methods, along with multiple variously oriented cores, to characterize any elastic anisotropy resulting from preferred orientation of the thermal cracks (cf., Mallet et al., 2013) and its pressure and frequency dependence;

6. More extensive measurements of permeability with water of controlled chemical composition (especially pH) as pore fluid, and also with nonpolar fluids (e.g. pentane) of broadly similar compressibility and viscosity;
7. More intensive sampling of the low-P_d realm so critical for cracked media;
8. Investigation of the redistribution of fluid by crack-pore as well as crack-crack squirt;
9. Assessment of the performance of alternative models for fluid-saturated rocks including those describing squirt flow within the context of poroelastic theory (e.g., Dvorkin et al., 1995; Gurevich et al., 2010; Pride et al., 2004).

Acknowledgments

The authors gratefully acknowledge technical assistance at ANU by Harri Kokkonen and Hayden Miller, and Andrew Latimore, and at the University of Alberta by Randolf Kofmann. Y. L. acknowledges PhD scholarship support from the Australian National University, as well as research support by grant DP110101830 from the Australian Research Council to I. J. and D. R. S. The experiments at LBNL were supported by the Office of Science, Office of Basic Energy Sciences, Division of Chemical Sciences of the U.S. Department of Energy, under the US DOE contract DE-AC02-05CH11231. The manuscript was markedly improved in response to reviews by Jian-guo Zhao and Yves Guéguen. The data represented in the figures in this article are tabulated by Li (2016).

A1 Inference of Crack Density at Each Pressure From Elastic Moduli Deficits Relative to the "Background Medium"

For a medium containing thin spheroidal cracks with major and minor axes a and b, respectively, the elastic moduli depend on both the volume fraction of cracks (crack porosity ϕ) and their aspect ratio $\alpha = b/a$ combined in the crack density Γ. For a population of N cracks per unit volume of common aspect ratio α,

$$\Gamma = N < a^3 >= (3/4\pi)\phi/\alpha. \quad \text{(A1)}$$

The normalized compressive and shear compliances for an infinitely thin crack ($\alpha \to 0$), respectively, P and Q, derived by Eshelby's method, are

$$P = 4\left(1 - \nu_0{}^2\right)/3\pi\alpha(1 - 2\nu_0) \text{ and } Q = 8(1 - \nu_0)(5 - \nu_0)/15\pi\alpha(2 - \nu_0), \quad \text{(A2)}$$

where ν_0 is the Poisson's ratio of the background medium, that is, the solid containing (high-pressure) nonclosable porosity in this case. The combined impact on the elastic moduli of the population of individual inclusions is obtained by substitution of equation A2 into the differential effective medium scheme (Le Ravalec & Guéguen, 1996)

$$(1-\phi)\frac{1}{K}\frac{dK}{d\phi} = -P(\nu), \quad \text{(A3)}$$

$$(1-\phi)\frac{1}{G}\frac{dG}{d\phi} = -Q(\nu), \quad \text{(A4)}$$

with the initial conditions $K(\phi = 0) = K_0$ and $G(\phi = 0) = G_0$, where ϕ is porosity, K and G are the effective bulk and shear moduli, respectively, and $\nu = (3K - 2G)/(6K + 2G)$ is the effective Poisson's ratio. This set of coupled equations is applied progressively, that is, integrated from zero to the desired level of porosity, to obtain the effective bulk modulus K and Poisson's ratio ν for the cracked medium as functions of crack density Γ:

$$\frac{K}{K^{hp}} = \frac{(1-2\nu^{hp})e^{-16\Gamma/9}}{1-2\nu^{hp}e^{-8\Gamma/5}}, \quad \text{(A5)}$$

$$\frac{\nu}{\nu^{hp}} = e^{-8\Gamma/5}, \quad \text{(A6)}$$

where K^{hp} and ν^{hp} are the bulk modulus and the Poisson's ratio of the matrix inclusive of the (“high-pressure”) nonclosable porosity.
Equations A5 and A6 are strictly applicable only for cracks of common aspect ratio. However, we shall apply them in inversion of the observed pressure-dependent modulus deficits for an effective crack density $\Gamma(P)$, which accounts for the contributions to the modulus deficits of all cracks that remain open at pressure P. This inversion strategy for the effective crack density has been verified by independent modeling (David, 2012). Values of $\Gamma(P)$, thus determined, are fitted to a smooth interpolation function for use in equation A7 below.

Finally, note that expressions analogous to euations A5 and A6, but valid for arbitrarily large aspect ratios, are used to invert the residual modulus deficits at P_{max} for the effective aspect ratio for the known amount of nonclosable porosity for each of the glass bead specimens. For additional details, refer to David and Zimmerman (2012).

A2 Computation of Aspect Ratio Distribution

The relationship between the pressure-dependent effective crack density $\Gamma(P)$ and the distribution of crack aspect ratios was initially developed by Morlier (1971), using the noninteractive dilute crack approximation for relating crack density to effective elastic moduli, and subsequently by Zimmerman (1991), using the differential effective medium scheme. In this analysis, the compressibilities of cracks of given aspect ratio and hence of the population of all open cracks are related to the measurable compressibility $C_{bc}(P)$ of the bulk cracked medium, and the compressibility of the medium containing only nonclosable pores, for which the bulk compressibility $C_{bc}{}^{hp}$ at P_{max} is a proxy. With this approach, the relationship between zero-pressure crack aspect ratio and closure pressure becomes

$$\alpha^{i} = \frac{3}{4\pi}\int_0^P \frac{\left[C_{bc}(P) - C_{bc}^{hp}\right]}{\Gamma(\alpha^{i})}\,dP, \quad \text{(A7)}$$

where $\Gamma(\alpha^{i})$ is the effective crack density associated with all cracks with zero-pressure aspect ratio $>\alpha^{i}$, which remain open at pressure P. A change of variable from P to Γ, results in (David & Zimmerman, 2012)

$$\alpha^{i} = \frac{3}{4\pi}\int_{\Gamma^{i}}^{\Gamma(\alpha)} \frac{\left[C_{bc}(\Gamma) - C_{bc}^{hp}\right]}{\Gamma}\frac{dP}{d\Gamma}\,d\Gamma, \quad \text{(A8)}$$

and $$\gamma(\alpha) = -\frac{d\Gamma}{d\alpha}. \quad \text{(A9)}$$

In equations A8 and A9, the bulk compressibility of the cracked medium is related to the observed P and S wave speeds as $C_{bc} = \frac{1}{K} = \left[\rho\left(V_p^2 - \frac{4}{3}V_s^2\right)\right]^{-1}$, and $\gamma(\alpha)$ is defined as the aspect ratio distribution function for the crack density. Finally, through the relationship between crack porosity and crack density (equation A1) at aspect ratio α, an aspect ratio distribution function $c(\alpha)$ for crack porosity is defined as

$$c(\alpha) = 4\pi\alpha\gamma(\alpha)/3, \quad \text{(A10)}$$

and the cumulative crack porosity $C(\alpha)$ as

$$C(\alpha) = \int_0^{\alpha} c(\alpha)\,d\alpha. \quad \text{(A11)}$$

Appendix B: Characteristic Frequency for Draining

From the differential equation governing the diffusion of pore fluid pressure P_f,

$$\nabla^2 P_f = (\phi\eta C_t/k)\partial P_f/\partial t, \quad \text{(A12)}$$

it has been directly inferred that the characteristic timescale τ for pore pressure equilibration over a length scale l is

$$\tau \cong \eta\phi l^2 C_t/k \quad \text{(A13)}$$

(Zimmerman, 1991, eq. 6.8). In equations A12 and A13, the total pore compressibility $C_t = C_f + C_{pp}$ is the sum of the fluid compressibility $C_f = K_f^{-1}$ and the pore compressibility $C_{pp} = (1/V_p)(\partial V_p/\partial P_p)_{Pc}$. With

$$C_{pp} = C_{pc} - C_r \cong C_{pc} \cong 2(1-\nu)/\pi\alpha G \quad \text{(A14)}$$

for cracks of low aspect ratio α (Zimmerman, 1991, eqs. 2.2 and 10.5) in a medium of compressibility C_r, and $C_{pc} = (-1/V_p)(\partial V_p/\partial P_c)_{Pp}$ (Zimmerman, 1991, eq. 1.7), it follows that the draining frequency f_{dr} is

$$f_{dr} = \tau^{-1} \cong \left(kK_f/\phi\eta l^2\right)/(1 + 2(1-\nu)K_f/\pi\alpha G). \quad \text{(A15)}$$

Equation A13 is identical to the well-known expression of Cleary (1978, eq. 3.5a) provided that Cleary's “appropriate modulus of the mixture” is

identified as $L_m = (4\phi C_t)^{-1}$. In the two limiting cases in which the total pore compressibility C_t is dominated by either C_f or C_{pp}, equation A15 takes the form given by equations 4a and 4b, respectively.

Appendix C: Computation of Fluid-Saturated Elastic Moduli at Each Pressure, Using the Differential Effective Medium Model

For this purpose, the right-hand sides of equations A3 and A4 are modified to incorporate fluid properties, becoming $-P_u(1-\xi)$ and $-Q_u$, respectively, where P_u and Q_u are complicated expressions for the normalized compressive and shear compliances of the undrained spheroidal inclusion which depend on α, ν, and ξ (David, 2012), and $\xi = K_f/K(\phi)$ is the ratio between the fluid bulk modulus and the effective bulk modulus at the current level of porosity. These coupled equations are then solved *iteratively* through a thought experiment, in which cracks in the fluid-saturated medium are reopened stepwise with decreasing pressure from P_{max}. The newly reopened cracks are progressively incorporated into the matrix that accordingly evolves with decreasing pressure (David & Zimmerman, 2012). As for the dry case, the "background matrix" includes the nonclosable pores; in the fluid-saturated case, the effect of nonclosable pores on the elastic moduli is calculated as described above for cracks, with appropriately chosen values of fluid-saturated normalized compressive and shear compliances (P_u, Q_u), using the value of aspect ratio for equant pores previously inferred from the deficits in dry, high-pressure moduli.

References

Adam, L., & Batzle, M. (2008). Elastic properties from laboratory measurements at seismic and ultrasonic frequencies. *The Leading Edge*, 27(8), 1026– 1032.

Adam, L., Batzle, M., & Brevik, I. (2006). Gassmann's fluid substitution and shear modulus variability in carbonates at laboratory seismic and ultrasonic frequencies. *Geophysics*, 71(6), F173– F183. https://doi.org/10.1190/1.2358494

Adam, L., Batzle, M., Lewallen, K. T., & van Wijk, K. (2009). Seismic wave attenuation in carbonates. *Journal of Geophysical Research*, 114, B06208. https://doi.org/10.1029/2008JB005890

Adelinet, M., Fortin, J., & Guéguen, Y. (2011). Dispersion of elastic moduli in a porous-cracked rock: Theoretical predictions for squirt-flow. *Tectonophysics*, 503(1-2), 173– 181. https://doi.org/10.1016/j.tecto.2010.10.012

Adelinet, M., Fortin, J., Guéguen, Y., Schubnel, A., & Geoffroy, L. (2010). Frequency and fluid effects on elastic properties of basalt: Experimental investigations. *Geophysical Research Letters*, 37, L02303. https://doi.org/10.1029/2009GL041660

Amalokwu, K., Best, A. I., Sothcott, J., Chapman, M., Minshull, T., & Li, X.-Y. (2014). Water saturation effects on elastic wave attenuation in porous rocks with aligned fractures. *Geophysical Journal International*, 197(2), 943– 947. https://doi.org/10.1093/gji/ggu076

Arena, A., Delle Piane, C., & Sarout, J. (2014). A new computational approach to crack quantification from 2D image analysis: Application to microcracks in rocks. *Computers and Geosciences*, 66, 106– 120.

Baechle, G. T., Weger, R. J., Eberli, G. P., Massaferro, J. L., & Sun, Y.-F. (2005). Changes of shear moduli in carbonate rocks: Implications for Gassmann applicability. *The Leading Edge*, 24(5), 507– 510. https://doi.org/10.1190/1.1926808

Bakhorji, A. (2010). Laboratory measurements of the static and dynamic elastic properties in carbonate, (PhD thesis, 368 pp.). University of Alberta.

Batzle, M. L., Han, D., & Hofmann, R. (2006). Fluid-mobility and frequency-dependent seismic velocity—Direct measurements. *Geophysics*, 71(1), N1– N9. https://doi.org/10.1190/1.2159053

Benson, P. M., Meredith, P. G., & Schubnel, A. (2006). Role of void space geometry in permeability evolution in crustal rocks at elevated pressure. *Journal of Geophysical Research*, 111, B12203. https://doi.org/10.1029/2006JB004309

Bernabé, Y., Lin, M., Tang, Y.-B., & Evans, B. (2016). Pore space connectivity and the transport properties of rocks, Oil Gas. Sci. Technol. – Rev. IFP, 71, 50.

Biot, M. A. (1956a). Theory of propagation of elastic waves in a fluid-saturated porous solid—I: Lower frequency range. *The Journal of the Acoustical Society of America*, 28(2), 168– 178. https://doi.org/10.1121/1.1908239

Biot, M. A. (1956b). Theory of propagation of elastic waves in a fluid-saturated porous solid—II: Higher frequency range. *The Journal of the Acoustical Society of America*, 28(2), 179– 191. https://doi.org/10.1121/1.1908241

Bouzidi, Y., & Schmitt, D. R. (2009). Measurement of the speed and attenuation of the Biot slow wave using a large ultrasonic transmitter. *Journal of Geophysical Research*, 114, B08201. https://doi.org/10.1029/2008JB006018

Brace, W. F., Walsh, J. B., & Frangos, W. T. (1968). Permeability of granite under high pressure. *Journal of Geophysical Research*, 73(6), 2225– 2236. https://doi.org/10.1029/JB073i006p02225

Cadoret, T., Marion, D., & Zinszner, B. (1995). Influence of frequency and fluid distribution on elastic-wave velocities in partially saturated

limestones. *Journal of Geophysical Research*, 100(B6), 9789– 9803. https://doi.org/10.1029/95JB00757

Chapman, M., Zatsepin, S. V., & Crampin, S. (2002). Derivation of a microstructural poroelastic model. *Geophysical Journal International*, 151(2), 427– 451. https://doi.org/10.1046/j.1365-246X.2002.01769.x

Cleary, M. P. (1978). Elastic and dynamic response regimes of fluid-impregnated solids with diverse microstructures. *International Journal of Solids and Structures*, 14(10), 795– 819. https://doi.org/10.1016/0020-7683(78)90072-0

Cline, C. J. II, & Jackson, I. (2016). Relaxation of the bulk modulus in partially molten dunite? *Geophysical Research Letters*, 43(22), 11,644– 11,651. https://doi.org/10.1002/2016GL071004

David, E. C. (2012). The effect of stress, pore fluid and pore structure on elastic wave velocities in sandstones, (PhD thesis). Imperial College London.

David, E. C., Fortin, J., Schubnel, A., Guéguen, Y., & Zimmerman, R. W. (2013). Laboratory measurements of low- and high-frequency elastic moduli in Fontainebleau sandstone. *Geophysics*, 78(5), D369– D379. https://doi.org/10.1190/geo2013-0070.1

David, E. C., & Zimmerman, R. W. (2011). Elastic moduli of solids containing spheroidal pores. *International Journal of Engineering Science*, 49(7), 544– 560. https://doi.org/10.1016/j.ijengsci.2011.02.001

David, E. C., & Zimmerman, R. W. (2012). Pore structure model for elastic wave velocities in fluid-saturated sandstones. *Journal of Geophysical Research*, 117, B07210. https://doi.org/10.1029/2012JB009195

Delle Piane, C., Arena, A., Sarout, J., Esteban, L., & Cazes, E. (2015). Micro-crack enhanced permeability in tight rocks: An experimental and microstructural study. *Tectonophysics*, 665, 149– 156. https://doi.org/10.1016/j.tecto.2015.10.001

Delle Piane, C., Sarout, J., Madonna, C., Saenger, E. H., Dewhurst, D. N., & Raven, M. (2014). Frequency-dependent seismic attenuation in shales: experimental results and theoretical analysis. *Geophysical Journal International*, 198(1), 504– 515. https://doi.org/10.1093/gji/ggu148

Ding, P., Di, B., Wang, D., Wei, J., & Li, X. (2014). P and S wave anisotropy in fractured media: experimental research using synthetic samples. *Journal of Applied Geophysics*, 109, 1– 6. https://doi.org/10.1016/j.jappgeo.2014.07.005

Domenico, S. N. (1977). Elastic properties of unconsolidated porous sand reservoirs. *Geophysics*, 42(7), 1339– 1368. https://doi.org/10.1190/1.1440797

Dullien, F. A. L. (1992). *Porous media: Fluid transport and pore structure*. San Diego, CA: Academic Press.

Dunn, K. J. (1986). Acoustic attenuation in fluid-saturated porous cylinders at low frequencies. *The Journal of the Acoustical Society of America*, 79(6), 1709– 1721. https://doi.org/10.1121/1.393232

Dunn, K. J. (1987). Sample boundary effect in acoustic attenuation of fluid-saturated porous cylinders. *The Journal of the Acoustical Society of America*, 81(5), 1259– 1266. https://doi.org/10.1121/1.394529

Dvorkin, J., Mavko, G., & Nur, A. (1995). Squirt flow in fully saturated rocks. *Geophysics*, 60(1), 97– 107. https://doi.org/10.1190/1.1443767

Dvorkin, J., Nolen-Hoeksema, R., & Nur, A. (1994). The squirt-flow mechanism: Macroscopic description. *Geophysics*, 59(3), 428– 438. https://doi.org/10.1190/1.1443605

Dvorkin, J., & Nur, A. (1993). Dynamic poroelasticity: A unified model with the squirt and the Biot mechanisms. *Geophysics*, 58(4), 524– 533. https://doi.org/10.1190/1.1443435

Endres, A. L., & Knight, R. J. (1997). Incorporating pore geometry and fluid pressure communication into modeling the elastic behavior of porous rocks. *Geophysics*, 62(1), 106– 117. https://doi.org/10.1190/1.1444110

Eshelby, J. D. (1957). The determination of the elastic field of an ellipsoidal inclusion, and related problems. *Proceedings of the Royal Society of London. Series A: Mathematical and Physical Sciences*, 241(1226), 376– 396. https://doi.org/10.1098/rspa.1957.0133

Fortin, J., Pimienta, L., Guéguen, Y., Schubnel, A., David, E. C., & Adelinet, M. (2014). Experimental results on the combined effects of frequency and pressure on the dispersion of elastic waves in porous rocks. *The Leading Edge*, 33(6), 648– 654. https://doi.org/10.1190/tle33060648.1

Gassmann, F. (1951). Uber die Elasticität Poröser Medien [On the elasticity of porous media]. *Vierteljahrsschrift der Naturforschenden Gesellschaft in Zürich*, 96, 1– 23.

Gregory, A. R. (1976). Fluid saturation effects on dynamic elastic properties of sedimentary rocks. *Geophysics*, 41(5), 895– 921. https://doi.org/10.1190/1.1440671

Guéguen, Y., & Palciauskas, V. (1994). *Introduction to the physics of rocks*. Princeton, NJ: Princeton University Press.

Guéguen, Y., & Sarout, J. (2011). Characteristics of anisotropy and dispersion in cracked medium. *Tectonophysics*, 503(1-2), 165– 172. https://doi.org/10.1016/j.tecto.2010.09.021

Gurevich, B., Makarynska, D., de Paula, O. B., & Pervukhina, M. (2010). A simple model for squirt-flow dispersion and attenuation in fluid-saturated granular
rocks. *Geophysics*, 75(6), N109– N120. https://doi.org/10.1190/1.3509782

Jackson, I. (1991). The petrophysical basis for the interpretation of seismological models for the continental lithosphere. *Special Publication. Geological Society of Australia*, 17, 81– 114.

Jackson, I. (2015). Properties of rocks and minerals-physical origins of anelasticity and attenuation in rock. In G. Schubert (Ed.), *Treatise on geophysics* (2nd ed., Vol. 2,
pp. 539– 571). Oxford. https://doi.org/10.1016/B978-0-444-53802-4.00045-2

Jackson, I., & Paterson, M. S. (1993). A high-pressure, high-temperature apparatus for studies of seismic wave dispersion and attenuation. *Pure and Applied Geophysics*, 141(2-
4), 445– 466. https://doi.org/10.1007/BF00998339

Jackson, I., Schijns, H., Schmitt, D. R., Mu, J., & Delmenico, A. (2011). A versatile facility for laboratory studies of viscoelastic and poroelastic behaviour of rocks. *The Review of Scientific Instruments*, 82(6), 064501. https://doi.org/10.1063/1.3592154

Johnson, D. L., & Plona, T. J. (1982). Acoustic slow waves and the consolidation transition. *The Journal of the Acoustical Society of America*, 72(2), 556– 565. https://doi.org/10.1121/1.388036

Jones, T. D., & Nur, A. (1983). Velocity and attenuation in sandstone at elevated temperatures and pressures. *Geophysical Research Letters*, 10(2), 140– 143. https://doi.org/10.1029/GL010i002p00140

Kachanov, M. (1993). Elastic solids with many cracks and related problems. *Advances in Applied Mechanics*, 30, 259– 445. https://doi.org/10.1016/S0065-2156(08)70176-5

King, M. S. (1966). Wave velocities in rocks as a function of changes in overburden pressure and pore fluid
saturants. *Geophysics*, 31(1), 50– 73. https://doi.org/10.1190/1.1439763

King, M. S., & Marsden, J. R. (2002). Velocity dispersion between ultrasonic and seismic frequencies in brine-saturated reservoir
sandstones. *Geophysics*, 67(1), 254– 258. https://doi.org/10.1190/1.1451700

King, M. S., Marsden, J. R., & Dennis, J. W. (2000). Biot dispersion for P- and S-wave velocities in partially and fully saturated sandstones. *Geophysical Prospecting*, 48(6), 1075– 1089. https://doi.org/10.1111/j.1365-2478.2000.00221.x

Kuster, G. T., & Toksöz, M. N. (1974). Velocity and attenuation of seismic waves in two-phase media: Part I. Theoretical

formulations. *Geophysics*, 39(5), 587– 606. https://doi.org/10.1190/1.1440450

Le Ravalec, M., & Guéguen, Y. (1996). High- and low-frequency elastic moduli for a saturated porous/cracked rock—Differential self-consistent and poroelastic theories. *Geophysics*, 61(4), 1080– 1094. https://doi.org/10.1190/1.1444029

Li, Y. (2016). A broadband laboratory study of the seismic properties of cracked and fluid-saturated synthetic glass materials, (PhD thesis). Australian National University.

Li, Y., Olin, M., David, E. C., Jackson, I., Schijns, H., & Schmitt, D. R. (2014). Broadband laboratory measurements of dispersion in thermally cracked and fluid-saturated quartzite and a synthetic analogue. *The Leading Edge*, 33(6), 624– 632. https://doi.org/10.1190/tle33060624.1

Lu, C., & Jackson, I. (2006). Low-frequency seismic properties of thermally cracked and argon-saturated granite. *Geophysics*, 71, F147– F159.

Mallet, C., Fortin, J., Guéguen, Y., & Bouyer, F. (2013). Effective elastic properties of cracked solids: An experimental investigation. *Geophysical Prospecting*, 61, 302– 314.

Mavko, G., & Jizba, D. (1991). Estimating grain-scale fluid effects on velocity dispersion in rocks. *Geophysics*, 56(12), 1940– 1949. https://doi.org/10.1190/1.1443005

Mavko, G., & Nur, A. (1975). Melt squirt in the asthenosphere. *Journal of Geophysical Research*, 80(11), 1444– 1448. https://doi.org/10.1029/JB080i011p01444

McCann, C., Sothcott, J., & Best, A. I. (2014). A new laboratory technique for determining the compressional wave properties of marine sediments at sonic frequencies and in situ pressure. *Geophysical Prospecting*, 62(1), 97– 116. https://doi.org/10.1111/1365-2478.12079

Melendez-Martinez, J., & Schmitt, D. R. (2016). A comparative study of the anisotropic dynamic and static elastic moduli of unconventional reservoir shales: Implications for geomechanical investigations. *Geophysics*, 81(3), D245– D261. https://doi.org/10.1190/geo2015-0427.1

Mikhaltsevitch, V., Lebedev, M., & Gurevich, B. (2014). A laboratory study of low-frequency wave dispersion and attenuation in water-saturated sandstones. *The Leading Edge*, 33(6), 616– 622. https://doi.org/10.1190/tle33060616.1

Morlier, P. (1971). Description de l'état de fissuration d'une roche à partir d'essais non-destructifs simples. *Rock Mechanics*, 3(3), 125– 138. https://doi.org/10.1007/BF01238439

Murphy, W. F. (1982). Effects of partial water saturation on attenuation in Massilon sandstone and Vycor porous glass. *The Journal of the Acoustical Society of America*, 71(6), 1458– 1468. https://doi.org/10.1121/1.387843

Murphy, W. F. (1984). Seismic to ultrasonic velocity drift: Intrinsic absorption and dispersion in crystalline rock. *Geophysical Research Letters*, 11(12), 1239– 1242. https://doi.org/10.1029/GL011i012p01239

Nakagawa, S. (2011). Split Hopkinson resonant bar test for sonic-frequency acoustic velocity and attenuation measurements of small, isotropic geological samples. *The Review of Scientific Instruments*, 82(4), 044901. https://doi.org/10.1063/1.3579501

Nakagawa, S., Kneafsey, T. J., Daley, T. M., Freifeld, B. M., & Rees, E. V. (2013). Laboratory seismic monitoring of supercritical CO_2 flooding in sandstone cores using the Split Hopkinson Resonant Bar technique with concurrent X-ray Computed Tomography imaging. *Geophysical Prospecting*, 61(2), 254– 269. https://doi.org/10.1111/1365-2478.12027

Nowick, A. S., & Berry, B. S. (1972). *Anelastic Relaxation in Crystalline Solids* (p. 677). New York and London: Academic Press.

Nur, A., Walls, J. D., Winkler, K., & De Vilbiss, J. (1980). Effects of fluid saturation on waves in porous rock and relations to hydraulic permeability. *SPE Journal*, 20(06), 450– 458. https://doi.org/10.2118/8235-PA

O'Connell, R. J., & Budiansky, B. (1977). Viscoelastic properties of fluid-saturated cracked solids. *Journal of Geophysical Research*, 82(36), 5719– 5735. https://doi.org/10.1029/JB082i036p05719

O'Hara, S. G. (1985). Influence of pressure, temperature, and pore fluid on the frequency-dependent attenuation of elastic waves in Berea sandstone. *Physical Review A*, 32(1), 472– 488. https://doi.org/10.1103/PhysRevA.32.472

O'Hara, S. G. (1989). Elastic-wave attenuation in fluid-saturated Berea sandstone. *Geophysics*, 54(6), 785– 788. https://doi.org/10.1190/1.1442707

Olin, M. (2011). Low-frequency seismic properties of synthetic sandstone, B. Eng. Thesis, Australian National University.

Ougier-Simonin, A., Guéguen, Y., Fortin, J., Schubnel, A., & Bouyer, F. (2011). Permeability and elastic properties of cracked glass under pressure. *Journal of Geophysical Research*, 116, B07203. https://doi.org/10.1029/2010JB008077

Palciauskas, V. V. (1992). Compressional to shear wave velocity ratio of granular rocks: Role of rough grain contacts. *Geophysical Research Letters*, 19(16), 1683– 1686. https://doi.org/10.1029/92GL01637

Palmer, I. D., & Traviolia, M. L. (1980). Attenuation by squirt flow in undersaturated gas sands. *Geophysics*, 45(12), 1780– 1792. https://doi.org/10.1190/1.1441065

Pandit, B. I., & King, M. S. (1979). The variation of elastic wave velocities and quality factor *Q* of a sandstone with moisture content. *Canadian Journal of Earth Sciences*, 16(12), 2187– 2195. https://doi.org/10.1139/e79-206

Pimienta, L., Fortin, J., & Guéguen, Y. (2014). Investigation of elastic weakening in limestone and sandstone samples from moisture adsorption. *Geophysical Journal International*, 199(1), 335– 347. https://doi.org/10.1093/gji/ggu257

Pimienta, L., Fortin, J., & Guéguen, Y. (2015a). Bulk modulus dispersion and attenuation in sandstones. *Geophysics*, 80(2), D111– D127. https://doi.org/10.1190/geo2014-0335.1

Pimienta, L., Fortin, J., & Guéguen, Y. (2015b). Experimental study of Young's modulus dispersion and attenuation in fully saturated sandstones. *Geophysics*, 80(5), L57– L72. https://doi.org/10.1190/geo2014-0532.1

Plona, T. J. (1980). Observation of a second bulk compressional wave in a porous medium at ultrasonic frequencies. *Applied Physics Letters*, 36(4), 259– 261. https://doi.org/10.1063/1.91445

Pride, S. R., Berryman, J. G., & Harris, J. M. (2004). Seismic attenuation due to wave-induced flow. *Journal of Geophysical Research*, 109, B01201. https://doi.org/10.1029/2003JB002639

Rathore, J. S. E., Fjaer, R. M. H., & Renlie, L. (1994). P- and S-wave anisotropy of a synthetic sandstone with controlled crack geometry. *Geophysical Prospecting*, 43, 711– 728.

Sarout, J. (2012). Impact of pore space topology on permeability, cut-off frequencies and validity of wave propagation theories. *Geophysical Journal International*, 189(1), 481– 492. https://doi.org/10.1111/j.1365-246X.2011.05329.x

Schijns, H., Jackson, I., & Schmitt, D. R. (2018). Shear modulus dispersion in cracked and fluid-saturated quartzites: Experimental observations and modeling. *Journal of Geophysical Research: Solid Earth*, 123. https://doi.org/10.1002/2017JB014633

Schneider, C. A., Rasband, W. S., & Eliceiri, K. W. (2012). NIH Image to ImageJ: 25 years of image analysis. *Nature Methods*, 9(7), 671– 675. https://doi.org/10.1038/nmeth.2089

Spencer, J. W. (1981). Stress relaxations at low frequencies in fluid-saturated rocks: Attenuation and modulus dispersion. *Journal of Geophysical Research*, 86(B3), 1803– 1812. https://doi.org/10.1029/JB086iB03p01803

Thévenaz, P., Ruttimann, U. E., & Unser, M. (1998). A pyramid approach to subpixel registration based on intensity. *IEEE Transactions on Image Processing*, 7(1), 27– 41. https://doi.org/10.1109/83.650848

Tillotson, P., Sothcott, J., Best, A. I., Chapman, M., & Li, X.-Y. (2012). Experimental verification of the fracture density and shear-wave splitting relationship using synthetic silica cemented sandstones with a controlled fracture geometry. *Geophysical Prospecting*, 60(3), 516– 525. https://doi.org/10.1111/j.1365-2478.2011.01021.x

Tittmann, B. R. (1978). Internal friction measurements and their implications in seismic Q structure models of the crust. In J. Heacock (Ed.), *The Earth's Crust*, Geophysical Monograph (6th ed., Vol. 20, pp. 197– 213). Washington, DC: American Geophysical Union.

Tutuncu, A. N., & Sharma, M. M. (1992). The influence of fluids on grain contact stiffness and frame moduli in sedimentary rocks. *Geophysics*, 57(12), 1571– 1582. https://doi.org/10.1190/1.1443225

Ulrich, T. J., McCall, K. R., & Guyer, R. A. (2002). Determination of elastic moduli of rock samples using resonant ultrasound spectroscopy. *The Journal of the Acoustical Society of America*, 111(4), 1667– 1674. https://doi.org/10.1121/1.1463447

Walsh, J. B. (1965). The effect of cracks on the compressibility of rock. *Journal of Geophysical Research*, 70(2), 381– 389. https://doi.org/10.1029/JZ070i002p00381

Wang, S. X., Zhao, J. G., Li, Z. H., Harris, J. M., & Quan, Y. (2011). Differential acoustic resonance spectroscopy for the acoustic measurement of small and irregular samples in the low frequency range. *Journal of Geophysical Research*, 117, B06203. https://doi.org/10.1029/2011JB008808

Wang, Z., Schmitt, D. R., & Wang, R. (2015). Does wettability influence seismic wave propagation in liquid-saturated porous rocks? *Geophysical Journal International*, 203(3), 2182– 2188. https://doi.org/10.1093/gji/ggv434

White, J. E. (1986). Biot-Gardner theory of extensional waves in porous rods. *Geophysics*, 51(3), 742– 745. https://doi.org/10.1190/1.1442126

Winkler, K. (1985). Dispersion analysis of velocity and attenuation in Berea sandstone. *Journal of Geophysical Research*, 90(B8), 6793– 6800. https://doi.org/10.1029/JB090iB08p06793

Winkler, K. (1986). Estimates of velocity dispersion between seismic and ultrasonic frequencies. *Geophysics*, 51(1), 183– 189. https://doi.org/10.1190/1.1442031

Winkler, K., & Nur, A. (1982). Seismic attenuation: Effects of pore fluids and frictional sliding. *Geophysics*, 47(1), 1– 15. https://doi.org/10.1190/1.1441276

Wu, T. T. (1966). The effect of inclusion shape on the elastic moduli of a two-phase material. *International Journal of Solids and Structures*, 2(1), 1– 8. https://doi.org/10.1016/0020-7683(66)90002-3

Wyllie, M. R. J., Gregory, A. R., & Gardner, L. W. (1956). Elastic wave velocities in heterogeneous and porous media. *Geophysics*, 21(1), 41– 70. https://doi.org/10.1190/1.1438217

Yin, C.-S., Batzle, M. L., & Smith, B. J. (1992). Effects of partial liquid/gas saturation on extensional wave attenuation in Berea sandstone. *Geophysical Research Letters*, 19(13), 1399– 1402. https://doi.org/10.1029/92GL01159

Zadler, B. J., Le Rousseau, J. H. L., Scales, J. A., & Smith, M. L. (2004). Resonant Ultrasound Spectroscopy: Theory and application. *Geophysical Journal International*, 156(1), 154– 169. https://doi.org/10.1111/j.1365-246X.2004.02093.x

Zhao, J. G., Tang, G. Y., Deng, J. X., Tong, X. L., & Wang, S. X. (2013). Determination of rock acoustic properties at low frequency: A differential acoustical resonance spectroscopy device and its estimation technique. *Geophysical Research Letters*, 40(12), 2975– 2982. https://doi.org/10.1002/grl.50346

Zhao, J. G., Wang, S. X., Tong, X. L., Yin, H., Yuan, D., Ma, X., et al. (2015). Differential acoustic resonance spectroscopy: improved theory and application in the low frequency range. *Geophysical Journal International*, 202(3), 1775– 1791. https://doi.org/10.1093/gji/ggv234

Zimmerman, R. W. (1991). *Compressibility of sandstones*. Amsterdam: Elsevier.